Universal Surface Passivation of Organic-Inorganic Halide Perovskite Films by Tetraoctylammonium Chloride for High Performance and Stable Perovskite Solar Cells

Seid Yimer Abate, Qiqi Zhang, Yifang Qi, Jawnaye Nash, Kristine Gollinger, Xianchun Zhu, Fengxiang Han, Nihar Pradhan, Qilin Dai\*

Department of Chemistry, Physics, and Atmospheric Sciences, Jackson State University, Jackson, MS, 39217, United States.

\* Corresponding author: Q. Dai, Email: qilin.dai@jsums.edu

#### Abstract

The power conversion efficiency of perovskite solar cells has been showing rapid improvement for the last decade. However, still, there is unarguable performance deficit compared with the Schockley-Queisser (SQ) limit. One of the major causes for such performance discrepancy is surface and grain boundaries defects. They are a source of non-radiative recombination in the devices not only causes performance loss but also the instability of the solar cells. In this study, we employed a direct post-surface passivation strategy at mild temperature to modify perovskite layer defects using tetraoctylammonium chloride (TOAC). The passivated perovskite layers have demonstrated extraordinary improvement in photoluminescence and charge carrier lifetimes compared to their control counterparts in both Cs0.05(FA0.83MA0.17)0.95Pb(I0.83Br0.17)3 and MAPbI3 type perovskite layers. The investigation on electron-only and hole-only devices after TOAC treatment revealed suppressed electron and hole trap density of states. The electrochemical study demonstrated that TOAC treatment improved the charge recombination resistance of the perovskite layers and reduced the charge accumulation on the surface of perovskite films. As a result, perovskite solar cells prepared by TOAC treatment showed a champion PCE of 21.24% for

Cs<sub>0.05</sub>(FA<sub>0.83</sub>MA<sub>0.17</sub>)<sub>0.95</sub>Pb(I<sub>0.83</sub>Br<sub>0.17</sub>)<sub>3</sub> – based device compared to 19.58% without passivation. Likewise, the PCE of MAPbI<sub>3</sub> improved from 18.09% to 19.27% with TOAC treatment. The long-term stability of TOAC passivated perovskite Cs<sub>0.05</sub>(FA<sub>0.83</sub>MA<sub>0.17</sub>)<sub>0.95</sub>Pb(I<sub>0.83</sub>Br<sub>0.17</sub>)<sub>3</sub> devices has retained over 97% of its initial performance after 720h in air.

## Keywords

Surface passivation, defects, traps, grain boundary, tetraoctylammonium chloride, perovskite solar cells

# Introduction

Organic-inorganic metal halide perovskites demonstrated outstanding photoelectric properties of high absorption coefficient, long carrier diffusion length, and fast electron and hole carrier mobility. Such novel materials incorporated in solar cells demonstrated a record power conversion efficiency (PCE) of above 25%.<sup>1, 2</sup> The perovskite composition, processing methods, processing conditions such as post annealing temperatures are among the parameters that determine the quality of perovskite film formation. Due to such unavoidable processing steps and conditions, various defects are formed on the perovskite film surface and grain boundaries.<sup>3</sup> These defects could be vacancies, interstitials, antistites or a combination of them.<sup>4,5</sup> Shallow level defects which are formed near the conduction band minimum or valence band maximum occupies a larger proportion of defects in perovskite film compared with the deep-level defects.<sup>6</sup> The defects could trap or scatter charge carriers. The trapped charge carriers by the defects influence the perovskite electrical, optical and charge carrier properties.<sup>5</sup>

In general, the defects present at the surface and grain boundaries of the perovskite film are the main source of non-radiative recombination which impacts the quantum efficiency of

photoluminescence in perovskite films and the photovoltaic parameters negatively.<sup>4, 7-13</sup> Defects are also a source of hysteresis where the electrons and holes that are trapped by defects under forward-bias are released under reverse-bias. Such slow charge trapping/de-trapping might cause photocurrent and photovoltage delay and lead to device hysteresis. Likewise, interstitial defects formed as a result of ion migration in perovskite films led to hysteresis.<sup>7, 14-16</sup> Furthermore, defects are the main causes of device instability where moisture and oxygen are infiltrated through surface defects and grain boundaries.<sup>6</sup> Thus, it is required to passivate the perovskite defects to boost the PCE, eliminate hysteresis and extend the device life.

So far, two kinds of passivation strategies are utilized to passivate the perovskite films: bulk treatment and surface treatment.<sup>9, 17</sup> In bulk treatment the passivation molecules are added directly to the perovskite precursor solution to get the treated perovskite layer. <sup>18, 19</sup> However, in the surface treatment the passivation molecules are deposited on the top of the perovskite layer (post surface treatment of perovskite layer). 20, 21 Form the ABX3 perovskite structure, A is cations, and B is metal (M<sup>+2</sup>), and X is the anion. This disclosed perovskite is ionic material and could form both positively V<sub>I</sub> and negatively V<sub>Pb</sub> charged defects. Due to the ionic nature of the perovskite material various passivation treatments are developed to passivate iodide vacancy, 3, 16, 22-26 chloride vacancy, 27-30 bromide vacancy, 31-33 and cation vacancy, 15, 26, 34-36 however, most of the previous findings heal one kind of defect only, either positively or negatively charged defect. For instance, from the reports on Lewis-base or Lewis-acid functional groups-based molecules to passivate perovskite, when the molecule has a Lewis-base functional group it only passivated positively charged V<sub>I</sub> defects <sup>37</sup>, and when the molecule is Lewis-acid functional group it only passivated negatively charged V<sub>Pb</sub> defects.<sup>38</sup> Considering from the large group of passivation materials, ammonium salts exhibited substantial advancements. 26, 35, 39-50 Tetrapropylammonium (TPA+)

cation enhanced both the surface and bulk passivation by forming strong ionic interaction with the surface of MAPbI<sub>3</sub> and via the formation of the heterostructure, respectively. <sup>10, 51</sup> Post-treatment of MAPbI<sub>3</sub> by Tetraoctylammonium bromide (TOAB) molecules effectively passivate the trap states at grain boundaries and surface.<sup>52</sup> Limited studies are about the passivation of both positively and negatively charged defects. 6, 13, 38, 53-56 The unsymmetric quaternary ammonium halides with a structure of NR<sub>4</sub><sup>+</sup>X<sup>-</sup> passivated both cationic and anionic defects.<sup>38</sup> Consequently, there is an urgent need to find a novel dual passivation molecule to modify both types of defects as they are always present in the perovskite film. Here for the first time, we used a symmetrical long-alkane chain quaternary ammonium halides of TOAC (TOA+Cl-) to passivate both the mixed perovskite (CsFAMA) and MAPbI<sub>3</sub>. The TOAC has an ionic nature thus it successfully passivated both the positively and negatively charged defects. The choice of TOAC molecule in our study is inspired by the previous success of quaternary ammonium salts of L-α-phosphatidylcholine and choline chloride to improve the performance and stability of perovskite solar cells. 11, 38 The zwitterionic TOAC is a symmetrical quaternary ammonium salt with a central eternally cationic nitrogen atom ((C<sub>8</sub>)<sub>4</sub>N<sup>+</sup>Cl<sup>-</sup>) and it is attached to long four alkyl chains. The oversized large ionic radius TOA<sup>+</sup> physiosorbed on the perovskite film through electrostatic interaction and treated not only the surface but also the perovskite grain boundaries to repress leakage, ion-migration and charge recombination pathways, consequently suppressing defects. <sup>25, 57</sup> The TOAC coordinates with the perovskite through hydrogen bonding to heal the I<sup>-</sup> and/or Br<sup>-</sup> vacancies thereby overcoming the non-radiative recombination pathways on the perovskite film. As a result, the treated perovskite exhibited improved photoluminescence (PL) and charge recombination resistance, which leads to improved V<sub>oc</sub> and FF.

Our experimental studies of the space-charge limited current (SCLC), photoluminescence (PL), time resolved photoluminescence (TRPL), and electrochemical impedance spectroscopy (EIS) have shown that TOAC significantly suppressed the number of defects, improved charge recombination resistance, and prolonged the carrier lifetime of the passivated CsFAMA and MAPbI<sub>3</sub> films/devices. Moreover, TOAC is a chemically stable charged molecule, with long alkyl chains are attached to it, which advances the hydrophobicity of the perovskite layer and enhances device long-term stability. Consequently, TOAC passivated PSCs devices exhibited a champion PCE of 21.24% concurrently with almost no PCE loss has been observed for devices kept in air (RH=40-55%) for 720 h.

#### **Experimental Section**

Materials: Fluorine tin oxide (FTO) substrates were purchased from Youxuan TECH, China. Tin(IV) oxide (SnO<sub>2</sub>), 15% in H<sub>2</sub>O colloidal dispersion bought from Alfa Aesar. Lead iodide (PbI<sub>2</sub>) and Lead Bromide (PbBr<sub>2</sub>) were purchased from TCI. Methylammonium iodide (MAI) was purchased from Xi'an Polymer Light Technology Corporation (China). Tetraoctylammonium chloride (TOAC), Formamidinium iodide (FAI), Cesium iodide, Methylammonium bromide (MABr), 2,2',7,7'-Tetrakis [N,N-di (4-methoxyphenyl)amino]-9,9'-spirobifluorene (Spiro-OMeTAD) and FK 209 Co(III) Li TFSI salt were purchased from Sigma-Aldrich. Lithium bis(trifluoromethanesulfony)imide (Li-TFSI) from TCI. 4-tert-butylpyridine (4-tBP) and were purchased from Accela. FK209 Co (III) Li-TFSI obtained from Greatcell materials. Poly[bis(4-phenyl)(2,4,6-trimethylphenyl)amine] (PTAA) was obtained from Solaris Chem (Canada). [6,6]-phenyl C61-butyric acid methyl ester (PC<sub>61</sub>BM) were purchased from Sigma-Aldrich. N,N-Dimethylformamide (DMF), isopropanol (IPA), acetonitrile (CAN) and chlorobenzene (CB) were

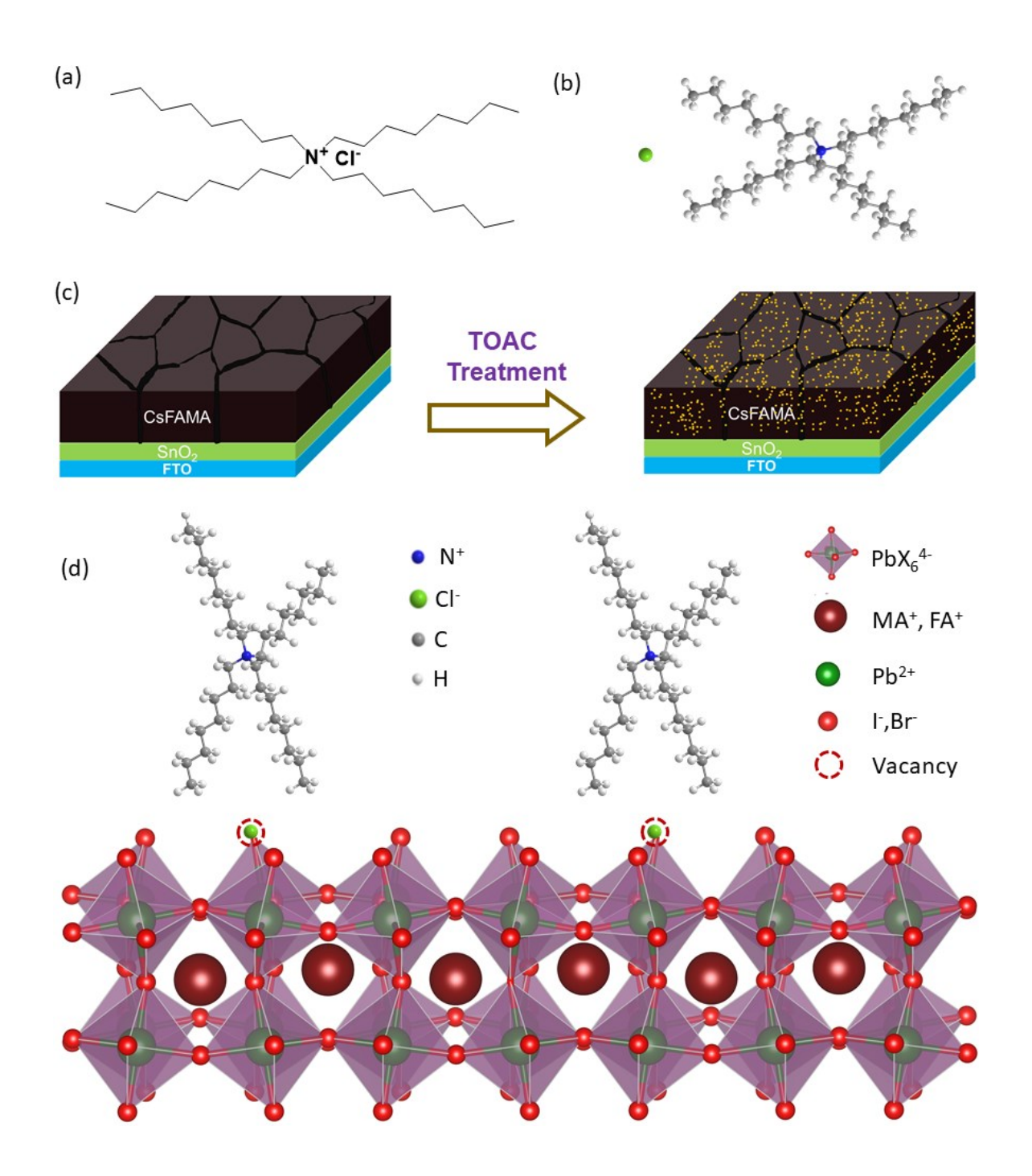
purchased from Sigma-Aldrich. Dimethyl sulfoxide (DMSO) was purchased from Alfa Aesar. Gold bar (Au 99.998%) were purchased from Alfa Aesar. All chemicals were used as received without further treatment.

Device Fabrication: Patterned FTO was sequentially cleaned as previously described.<sup>58</sup> SnO<sub>2</sub> ETL was prepared from a dispersion of Tin (IV) oxide colloidal to DI water (1:3 v/v) by spin coating and annealed at 150 °C for 30 min. The mixed perovskite with a composition of Cs<sub>0.05</sub>(FA<sub>0.83</sub>MA<sub>0.17</sub>)<sub>0.95</sub>Pb(I<sub>0.83</sub>Br<sub>0.17</sub>)<sub>3</sub> is prepared by mixing FAI (1 mM), PbI<sub>2</sub> (1.1 M), MABr (0.2 mM), PbBr<sub>2</sub> (0.2 mM) in DMF: DMSO (4:1 v/v). A stoichiometric amount of (40 μL) CsI from a solution of 1.5 mM CsI in DMSO was added to get the final composition. The mixed perovskite is deposited at 4000 rpm for 40 s and chlorobenzene was dropped as anti-solvent in the middle of the spinning procedure and subsequently annealed 100 °C for 1h. The MAPbI<sub>3</sub> is prepared following a literature. 52, 59 After that various concentrations of TOAC in 2-propanol were spin coated on perovskite layers at 4000 rpm for 30 s and annealed at a mild temperature of 70 °C for 10 min. The optimized TOAC concentration for the mixed perovskite is 2.5 mM, and for MAPbI<sub>3</sub> is 0.5 mM in 2-propanol. Unless concentration is specified, we have only discussed the concentrations in all discussions. Following, spiro-OMeTAD is deposited at 4000 rpm for 30 s from a solution of 90 g spiro-OMeTAD doped with 39.5µL TBP, 22.5µL Li-TFSI (52mg in 100µL acetonitrile), and 10µL FK 209 Co(III) Li TFSI (375 mg in 1mL acetonitrile). Finally, Au (~70 nm) was deposited by a thermal evaporator.

**Film and device characterizations:** The characterization of peovskite and modified perovskite films by XRD, FT-IR, SEM, UV-Vis, PL, TRPL and all I-V, EQE, and EIS device measurements were done using the apparatus described in reference.<sup>59, 60</sup>

## Results and discussion

The perovskite passivation strategy is illustrated in Scheme 1, where various concentrations of TOAC (Scheme 1a-b) in 2-propannol is spin coated on the perovskite layer following mild annealing at 70 °C (Scheme 1c). Scheme 1d shows the interaction between perovskite and TOAC. Here, we deeply studied the effect of TOAC passivation on mixed perovskite with a composition of Cs<sub>0.05</sub>(FA<sub>0.83</sub>MA<sub>0.17</sub>)<sub>0.95</sub>Pb(I<sub>0.83</sub>Br<sub>0.17</sub>)<sub>3</sub> and MAPbI<sub>3</sub> films. In the first section we describe TOAC influence on Cs<sub>0.05</sub>(FA<sub>0.83</sub>MA<sub>0.17</sub>)<sub>0.95</sub>Pb(I<sub>0.83</sub>Br<sub>0.17</sub>)<sub>3</sub>, then on MAPbI<sub>3</sub>. The preparation of the perovskite films is briefly explained in the experimental section.



Scheme 1. (a) Molecular structure of TOAC, (b) 3-D molecular geometry of TOAC, (c) schematic representation of TOAC passivation on CsFAMA, (d) Schematic illustration of interaction of perovskite and TOAC.

Initially, to understand the interaction between CsFAMA and TOAC, we recorded FTIR (Figure 1a-f) The FTIR peaks at 1472 cm<sup>-1</sup> (sym. NH<sub>3</sub><sup>+</sup> bend)<sup>61</sup>, both 3271 cm<sup>-1</sup> and 3407 cm<sup>-1</sup> ( N-H stretch)<sup>62</sup> of the control CsFAMA film are shifted to lower wavenumber of 1468 cm<sup>-1</sup>, 3161 cm<sup>-1</sup> and 3401 cm<sup>-1</sup>, respectively for CsFAMA / TOAC. Moreover, the peak at 2850 cm<sup>-1</sup> (sym. CH<sub>3</sub> rock)<sup>61</sup>, 2918 cm<sup>-1</sup> (sym. CH<sub>3</sub> stretch)<sup>61</sup>, and 2954 cm<sup>-1</sup> (asym. CH<sub>3</sub> stretch)<sup>52, 61</sup> of the TOAC molecule shifted to 2856 cm<sup>-1</sup>, 2926 cm<sup>-1</sup>, and 2957 cm<sup>-1</sup>, respectively for CsFAMA / TOAC which indicated the existence of strong chemical interaction between TOAC and CsFAMA.<sup>52, 60,</sup> 62, 63 The shifts of the NH<sub>3</sub><sup>+</sup> stretching and NH<sub>3</sub><sup>+</sup> bending to lower wavenumber clearly revealed that there are strong hydrogen bonding interactions between TOAC and CsFAMA through the NH<sub>3</sub><sup>+</sup> and TOAC (N-H···Cl). <sup>60, 61, 63, 64</sup> Additionally, the peaks at 1713 cm<sup>-1</sup> ( C=N)<sup>63</sup> for the CsFAMA shifted to 1709 cm<sup>-1</sup> upon TOAC passivation which additionally signifies the strong interaction between TOAC and CsFAMA.<sup>63, 64</sup> Moreover, the EDX elemental mapping images of CsFAMA / TOAC film (presented in Figure 1g) reveal that Cl atoms are distributed uniformly all over the CsFAMA surface. Therefore, both the FTIR and EDX mapping data demonstrate the successful incorporation of the TOAC into the perovskite layer. The full FTIR spectra and EDX elemental mapping for all elements of CsFAMA are presented in Figure S1 and Figure S2, respectively.

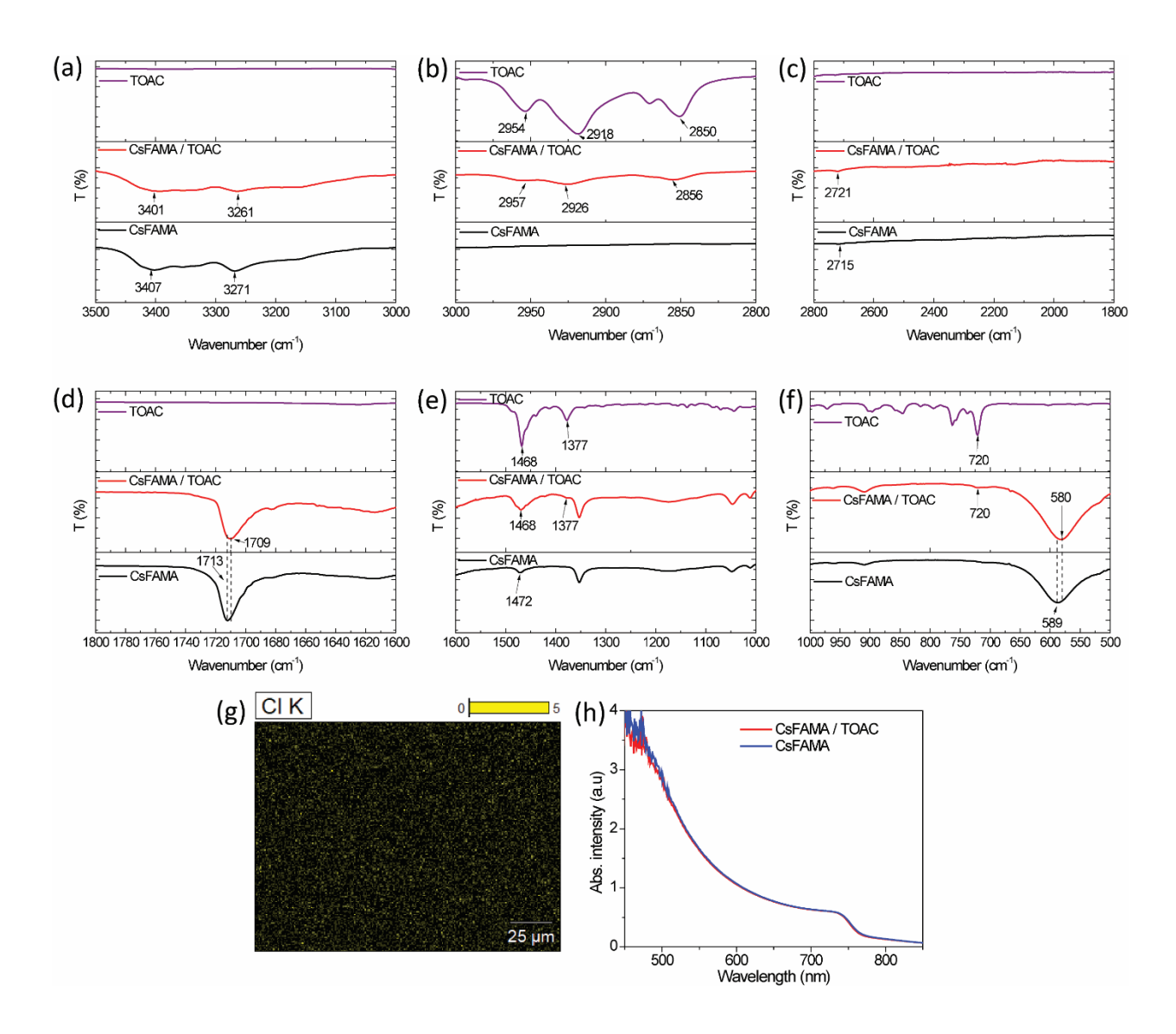


Figure 1. (a-f) FTIR of TOAC, CsFAMA and CsFAMA/ TOAC, (g) ESD elemental mapping of CsFAMA/ TOAC, and (h) UV-vis absorption of CsFAMA with and without TOAC.

The UV-Vis absorption of CsFAMA with and without TOAC treatment was deposited on glass and recorded, and both films showed similar absorption profiles in all wavelength ranges. (Figure 1h). This means the CsFAMA film thickness barely changed after TOAC treatment. Besides, both films exhibited an absorption onset at *ca.* 770 nm. The XRD of the control CsFAMA and CsFAMA / TOAC showed all the characteristic peaks of perovskite (Figure 2a). The XRD peak about 12. 6° is attributed to the excess PbI<sub>2</sub> added in the precursor solution to improve the PCE of the device.

Figure 2b and Figure 2c showed the top-view SEM images of CsFAMA with and without TOAC passivation, respectively. We have observed the presence of large pinholes and grain boundaries on the control sample SEM. Besides, there are many white crystals on the top surface of CsFAMA that are assigned to PbI<sub>2</sub>. However, the distributions of white crystals are reduced on the top view SEM of the passivated surface (Figure 2c), which are consistent with the PbI<sub>2</sub> XRD peak intensity decrement for the passivated CsFAMA. This strengthens our hypothesis that the TOAC incorporation in CsFAMA. Additionally, the CsFAMA grain sizes decreased after TOAC passivation and show flat and compact morphology. Similar grain size shrinkage have been observed when smaller ionic radius ammonium salts such as ethylammonium (EAI: 258 pm), imidazolium (258 pm) and guanidinium iodide (278 pm) used to treat mixed cation perovskite, compared to formamidinium, (253 pm) and methylammonium, (217 pm).<sup>65</sup> The solid state NMR, <sup>1</sup>H-<sup>1</sup>H spin diffusion measurement and solid-state <sup>1</sup>H MAS NMR confirmed that mixed cation perovskite treated with ethylammonium exhibited that the EAI is fully converted into EAcontaining lead halide phases during the passivation to treat the surface and grain bounderies.<sup>44</sup> However, when MAPbI<sub>3</sub> was treated by large ionic radius (450 pm) tetrapropylammonium (TPA<sup>+</sup>) cation the grain showed shrinkage, in which TPA<sup>+</sup> cannot be accommodated inside the lattice of the perovskite structure.<sup>51</sup> The addition of TPA<sup>+</sup> provokes a reduction of the cell volume mostly driven by a shrinkage along the [001] direction of the pure MAPbI<sub>3</sub>.<sup>51</sup> Likewise, TOAC cannot be incorporated inside the lattice of the perovskite structure and the grain could be smaller by the shrinkage in [001] direction. Formation of small grains, but, compact and flat morphologies are beneficial to achieve high open-circuit voltage (V<sub>oc</sub>) and fill factor (FF) in PSCs.<sup>26</sup> We study AFM to study the details in the flatness of the perovskite films before and after passivation. The top view AFM, 3-D AFM and AFM height of CsFAMA are presented in Figure 2d-f, and CsFAMA / TOAC

AFM data are shown in Figure 2g-i. The control sample has a roughness of 22.4 nm. The roughness significantly decreases to 16.6 nm after TOAC passivation, which is beneficial to achieving a

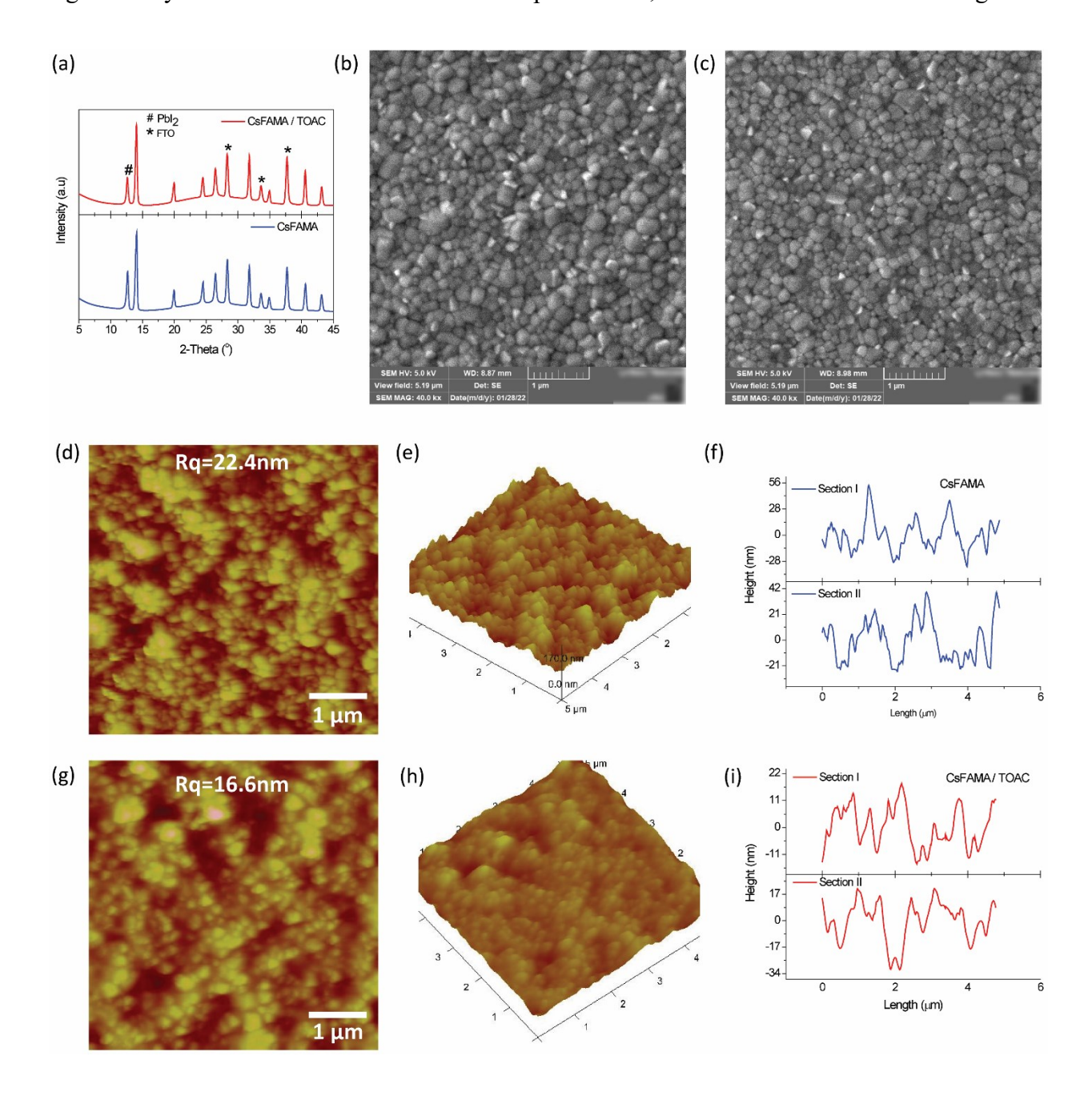


Figure 2. (a) XRD diffraction patterns of CsFAMA with and without TOAC, (b) Top view SEM image of CsFAMA, (c) Top view SEM image of CsFAMA / TOAC, (d-f) AFM surface image, 3-

dimentinal image and height image for CsFAMA, respectively. (g-i) AFM surface image, 3-dimentinal image and height image for CsFAMA/ TOAC, respectively.

smooth spiro-OMeTAD top layer. The AFM height images of CsFAMA and CsFAMA / TOAC across 5 µm film were measured and they clearly demonstrate smoother film was achieved by TOAC passivation. These results could be explained in two premises. First, the TOAC might react with the uncoordinated PbI<sub>2</sub> to form perovskite, <sup>44, 51, 52, 66</sup> and/or the TOAC infiltrate the grain boundaries and surface defects of CsFAMA flatten the surface.

The charge extraction properties of CsFAMA and CsFAMA / TOAC film are investigated by PL and TRPL. These films are prepared by spin coating the perovskite films on glass substrates, and the incident light is directed from the perovskite side. Figure 3a demonstrates the PL intensity of CsFAMA, CsFAMA / Spiro-OMeTAD, CsFAMA / TOAC and CsFAMA/TOAC/spiro-OMeTAD. CsFAMA / TOAC passivated film exhibits enhanced photoluminescence (almost double intensity) compared to the control CsFAMA. Trap states on the surface and grain boundaries of the CsFAMA film are suppressed by TOAC passivation. The TOAC molecules modify traps and grain boundaries so that the defect density decreases on the passivated CsFAMA, leading to enhanced photoluminescence. The traps and grain boundaries in the control film not only affect the photoluminescence but also will influence the cell performance and device hysteresis (we will discuss later). We record PL of the perovskite layers with and without TOAC passivation coated by spiro-OMeTAD. In both cases, the PL shows quenched. The CsFAMA / spiro-OMeTAD quenches 64%. The CsFAMA /TOAC /Spiro-OMeTAD film quenches more than 93%, which implies charge extraction from perovskite to spiro-OMeTAD enhanced by TOAC passivation. This displays the potential of TOAC on preventing nonradiative recombination in the perovskite films. The TRPL spectra of the control and passivated films are presented in Figure 3b. The

lifetimes are fitted by the biexponential function using equation (1), and the average lifetimes are calculated using equation (2). A<sub>1</sub> and A<sub>2</sub> are the relative amplitudes. t is time.  $\tau_1$  and  $\tau_2$  are the lifetime values for the fast and slow decay, respectively.

$$Y = A_1 \exp\left(\frac{-t}{\tau_1}\right) + A_2 \exp\left(\frac{-t}{\tau_2}\right)$$
 equation (1)

$$\tau_{avg} = \frac{A_1 \tau_1^2 + A_2 \tau_2^2}{A_1 \tau_1 + A_2 \tau_2}$$
 equation (2)

The average lifetime of control perovskite CsFAMA is 284.73 ns. After TOAC passivation, the lifetime CsFAMA / TOAC increases substantially to 376.36 ns. A longer lifetime of the CsFAMA / TOAC confirms the suppression of defects on the control sample after TOAC treatment. The lifetimes of CsFAMA/ Spiro-OMeTAD and CsFAMA/ TOAC/ Spiro-OMeTAD are also measured. CsFAMA/ TOAC/ Spiro-OMeTAD shows the shortest lifetime of 15.28 ns vs 26.45 ns for the CsFAMA/Spiro-OMeTAD. This displays the charge extraction of CsFAMA is improved after TOAC passivation. These results are consistent with the PL studies. The lifetime results are summarized in Table S1.

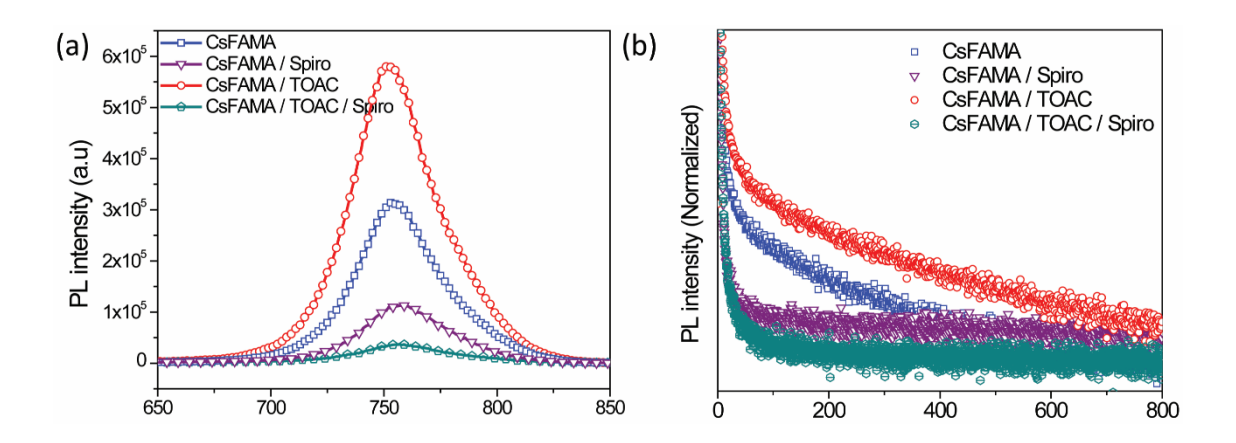


Figure 3. (a) Steady state PL and (b) TRPL of CsFAMA, CsFAMA/TOAC, CsFAMA/spiro-OMeTAD and CsFAMA/TOAC/spiro-OMeTAD.

Perovskite solar cells with a structure of FTO/SnO<sub>2</sub>/CsFAMA (with and without TOAC)/Spiro-OMeTAD/Au were fabricated to investigate the influence of TOAC on the photovoltaic property of the device. Cells are fabricated by spin coating various concentration of TOAC (0 mM, 0.5 mM, 1.0 mM, 1.5 mM, 2.0 mM, 2.5 mM and 3.0 mM) in 2-propanol on the CsFAMA film, and devices are characterized. Figure 4a showed the cross-sectional SEM of the full device with the optimized (2.5 mM) TOAC, where about 400 nm CsFAMA / TOAC is deposited on the SnO<sub>2</sub> layer. The TOAC passivated optimized device exhibits a champion reverse bias PCE of 21.24% with a J<sub>sc</sub> of 24.29 mAcm<sup>-2</sup>, V<sub>oc</sub> of 1.134 V, and FF of 77.12% (Figure 4b) and forward bias PCE of 20.77% with a J<sub>sc</sub> of 24.26 mAcm<sup>-2</sup>, V<sub>oc</sub> of 1.131 V, FF of 75.71%. Furthermore, it showed a stabilized power output 21.22% PCE while measured at maximum power point of 0.92 V (inset Figure 4b). However, the control device demonstrates a maximum reverse PCE of only 19.58% with a J<sub>sc</sub> of 23.46mAcm<sup>-2</sup>, V<sub>oc</sub> of 1.118 V, FF of 74.66% (Figure 4c), and forward PCE of 18.40% with a J<sub>sc</sub> of 23.57mAcm<sup>-2</sup>, V<sub>oc</sub> of 1.112 V, FF of 70.22%, with a stabilized power output 19.58% PCE while measured at maximum power point of 0.92 V (inset Figure 4c). The hysteresis index (HI) for the control film is 0.06. The HI declines down to 0.02 after passivation. The champion device photovoltaic parameters and hysteresis calculations are summarized in Table S2. To study the reproducibility of our fabrication above 25 CsFAMA and CsFAMA / TOAC -based solar cells are prepared and characterized (Figure 4d-g). The CsFAMA / TOAC device exhibits outstanding J<sub>sc</sub>, Voc, and FF compared to the standard CsFAMA device. The box-chart of J-V characteristics for all concentrations are presented in Figure S3 and the maximum PCE values for each concentration are summarized in Table S3. Generally, at low concentration (< 2 mM of TOAC) the average J<sub>sc</sub> and FF are improved upon passivation. However, the average V<sub>oc</sub> doesn't show improvement, even for some devices the Voc is decreased at a small concentration of TOAC treated device compared

to the standard device. At the optimized 2.5 mM TOAC all the device parameters (J<sub>sc</sub>, V<sub>oc</sub>, and FF) improved and the device exhibited its champion performance. However, further increases in the concentration of TOAC to 3.0mM decrease the J-V parameters. The EQE of the control and CsFAMA/ TOAC devices are presented in Figure 4h, where the integrated J<sub>sc</sub> of 20.80 mAcm<sup>-2</sup> and 21.13 mAcm<sup>-2</sup> are measured for CsFAMA and CsFAMA / TOAC-based devices, respectively. A discrepancy of *Ca.* 13% is observed between integrated J<sub>sc</sub> and J<sub>sc</sub> measured from I–V curve because the EQE measurement is carried out in a single wavelength with much lower intensity than the one sun radiation.<sup>67</sup> The integrated J<sub>sc</sub> extracted from I–V scans that is within 20% of the value calculated from EQE signifies a reasonable correlation.<sup>68</sup>

Figure 4(i) shows the electrical impedance spectroscopy (EIS) of the control and TOAC passivated devices. Here we investigate the charge recombination property of the control and CsFAMA / TOAC - devices at dark conditions at a bias of 0.92V. The equivalent circuit is shown in the inset of Figure 4i, where Rs is the series resistance from the ITO and wire, CPE1 is the contact capacitance of the perovskite film with its adjacent contacts,  $R_1$  is the dielectric relaxation resistance, CPE2 is the capacitance of perovskite films, and  $R_{\rm rec}$  is the charge recombination resistance of the cells. The EIS fitting parameters are summarized in Table S4. The results revealed that the capacitance of the control CsFAMA is four orders higher than the passivated CsFAMA, which implies the control device is affected by a serious charge buildup in perovskite that potentially facilitates nonradiative charge recombination in the cell to cause photoluminescence loss and device instability. The control device exhibited a charge recombination resistance ( $R_{\rm rec}$ ) of 1323  $\Omega$ , which enhances about three-fold after TOAC passivation to 3674  $\Omega$  that indeed demonstrates the potential of TOAC to suppress charge traps on the CsFAMA film.

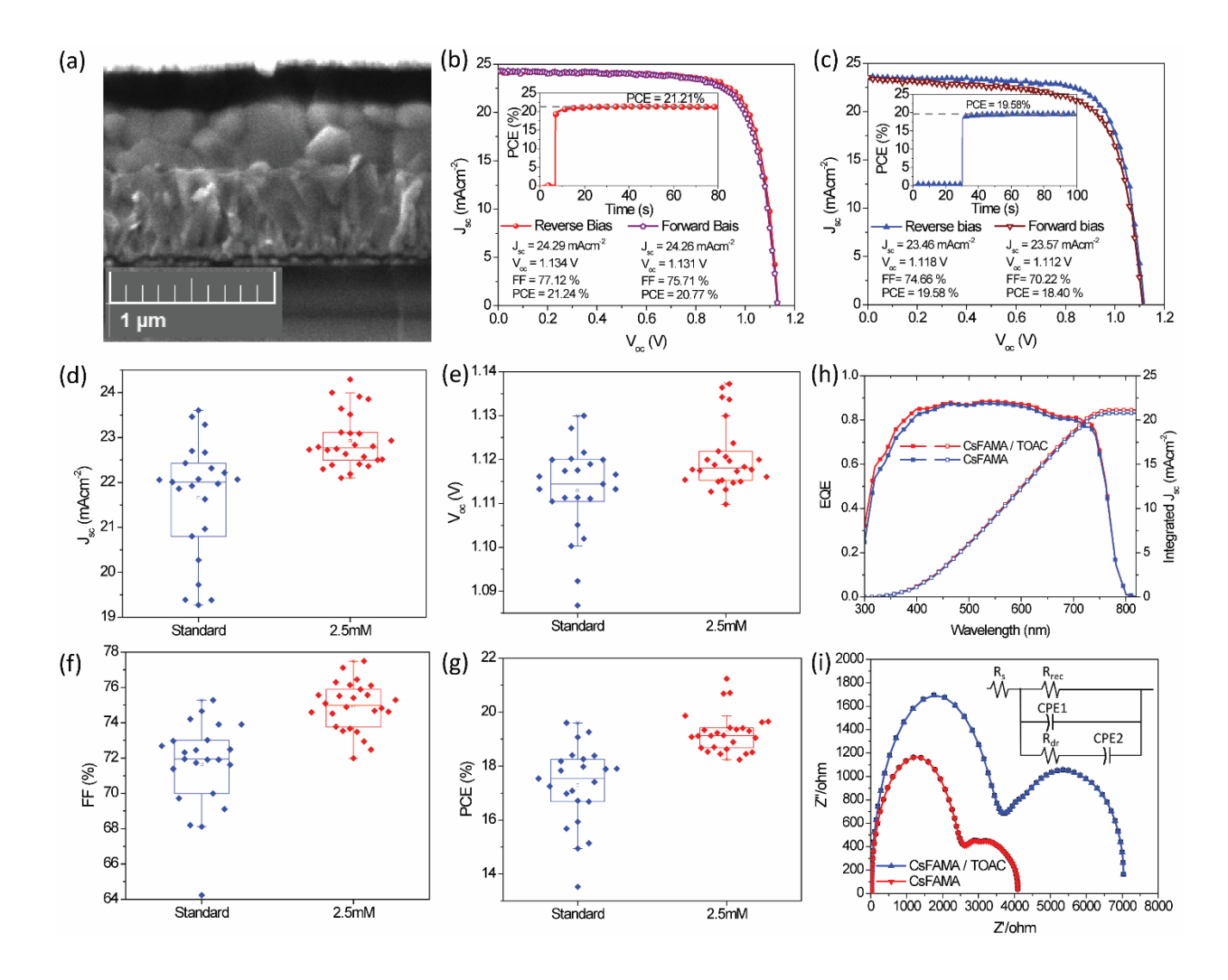


Figure 4. (a) Cross-sectional SEM of FTO/SnO<sub>2</sub>/CsFAMA/TOAC/Spiro-OMeTAD/Au. (b) The champion device fabricated using the optimized 2.5mM TOAC passivated CsFAMA. The inset in Figure 4(b) is the stabilized power output of CsFAMA / TOAC-based PSC devices measured at maximum power point of 0.92 V. (c) Reverse and forward bias J-V profile of the control device with a structure of FTO/SnO<sub>2</sub>/CsFAMA/Spiro-OMeTAD/Au. The inset in Figure 4(c) is the stabilized power output of the control devices measured at maximum power point of 0.92 V. Box chart comparison of the J-V parameters between the standard CsFAMA and 2.5mM TOAC passivated CsFAMA (d) J<sub>sc</sub>, (e) V<sub>oc</sub>, (f) FF and (g) PCE. (h) EQE of CsFAMA and CsFAMA/TOAC and (i)Nyquist plots of the device without and with 2.5mM TOAC passivated CsFAMA

The trap state density of CsFAMA and CsFAMA / TOAC based devices is further investigated by fabricating a single charge injection device of the electron-only device and hole-only device. The electron-only device with a structure of FTO/SnO<sub>2</sub>/CsFAMA (with and without TOAC)/PCBM/Au are employed to study electron trap, and hole-only device with a structure of FTO/PTAA/CsFAMA (with and without TOAC)/Spiro-OMeTAD/Au is used to characterize hole traps. The I-V characterizations (measured in dark conditions) are plotted on a double logarithmic graph as shown in Figure 5a-b. The trap state density of the respective devices is calculated using equation (3), where  $\varepsilon$  is the relative dielectric constant of CsFAMA (~79% composition is FAPbI<sub>3</sub>) then we adopt  $\varepsilon$  of FAPbI<sub>3</sub> (46.9)<sup>24, 69</sup>.  $\varepsilon$ <sub>0</sub> is vacuum permittivity. V<sub>TFL</sub> is trap-filled limit voltage. e is the elementary charge. L is the thickness of CsFAMA with and without TOAC and N<sub>traps</sub> is the number of traps.

$$N_{traps} = \frac{2\varepsilon\varepsilon_0 V_{TFL}}{eL^2}$$
 equation (3)

The N<sub>traps</sub> for the control electron-only device is  $11.3 \times 10^{15}$  cm<sup>-3</sup>. With TOAC passivation the electron traps are significantly reduced to  $6.48 \times 10^{15}$  cm<sup>-3</sup>. The N<sub>traps</sub> for the control hole-only device  $10.1 \times 10^{15}$  cm<sup>-3</sup>, and after passivation the traps slightly decrease to  $8.39 \times 10^{15}$  cm<sup>-3</sup>. From this, we can conclude that TOAC could passivate both the electron traps and hole traps. However, it passivates more electron traps than the hole traps. This means TOAC could passivate I<sup>-</sup> and/or Br<sup>-</sup> defects from Cs<sub>0.05</sub>(FA<sub>0.83</sub>MA<sub>0.17</sub>)<sub>0.95</sub>Pb(I<sub>0.83</sub>Br<sub>0.17</sub>)<sub>3</sub> composition than Pb<sup>2+</sup> defect. This phenomenon is similar to previous studies that add a small concentration of PbCl<sub>2</sub> into MAPbI<sub>3</sub> solution where the Cl<sup>-</sup> passivated both anion and cation defects. The density of the trap study is coherent with both the PL and EIS studies. The SCLC parameters are summarized in Table S5.

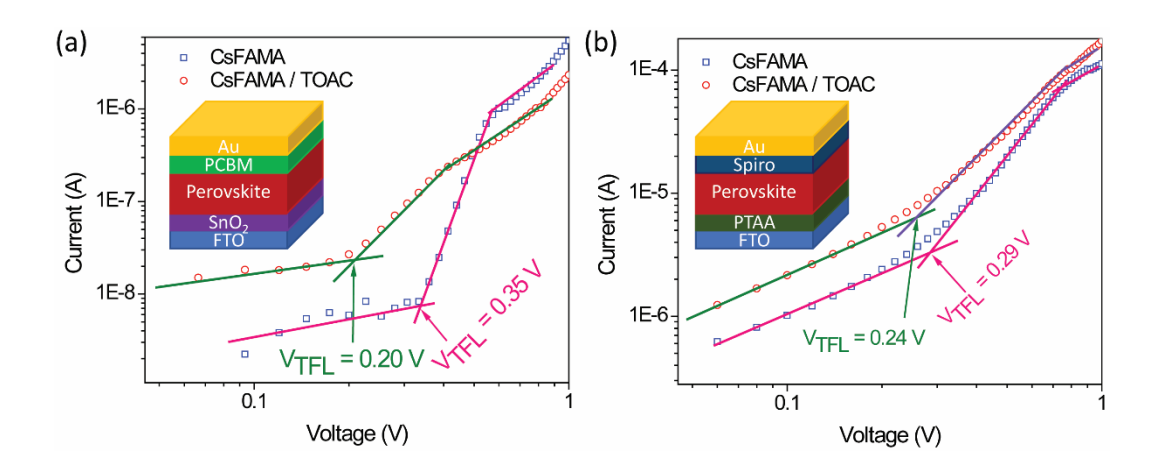


Figure 5. (a) Electron only device with a structure of FTO/SnO<sub>2</sub>/CsFAMA (with and without TOAC)/PCBM/Au, (b) hole only device with a structure of FTO/PTAA/CsFAMA (with and without TOAC)/Spiro-OMeTAD/Au.

Finally, we study the long-term stability of CsFAMA and CsFAMA / TOAC based devices in the air. Figures 6 a and b show the water contact angels of the CsFAMA and CsFAMA/TOAC films. It can be observed that the waver contact angle increases from 46.33° to 90.61°, which shows significant potential to achieve improved moisture stability of the devices. The devices have been kept in the air at (RH = 40-60%) in a dark condition for 720 hours. Four devices of the control and TOAC passivated devices are studied, and the results are summarized in Figure 6 c-f. The TOAC passivated devices show remarkable moisture stability compared to the control device. The TOAC devices retain an average of 97.61% of their initial PCE vs the controls only an average of 89.05% of their initial PCE. This demonstrates TOAC treatment not only improves the PCE but also enhances the long-term stability of the devices.

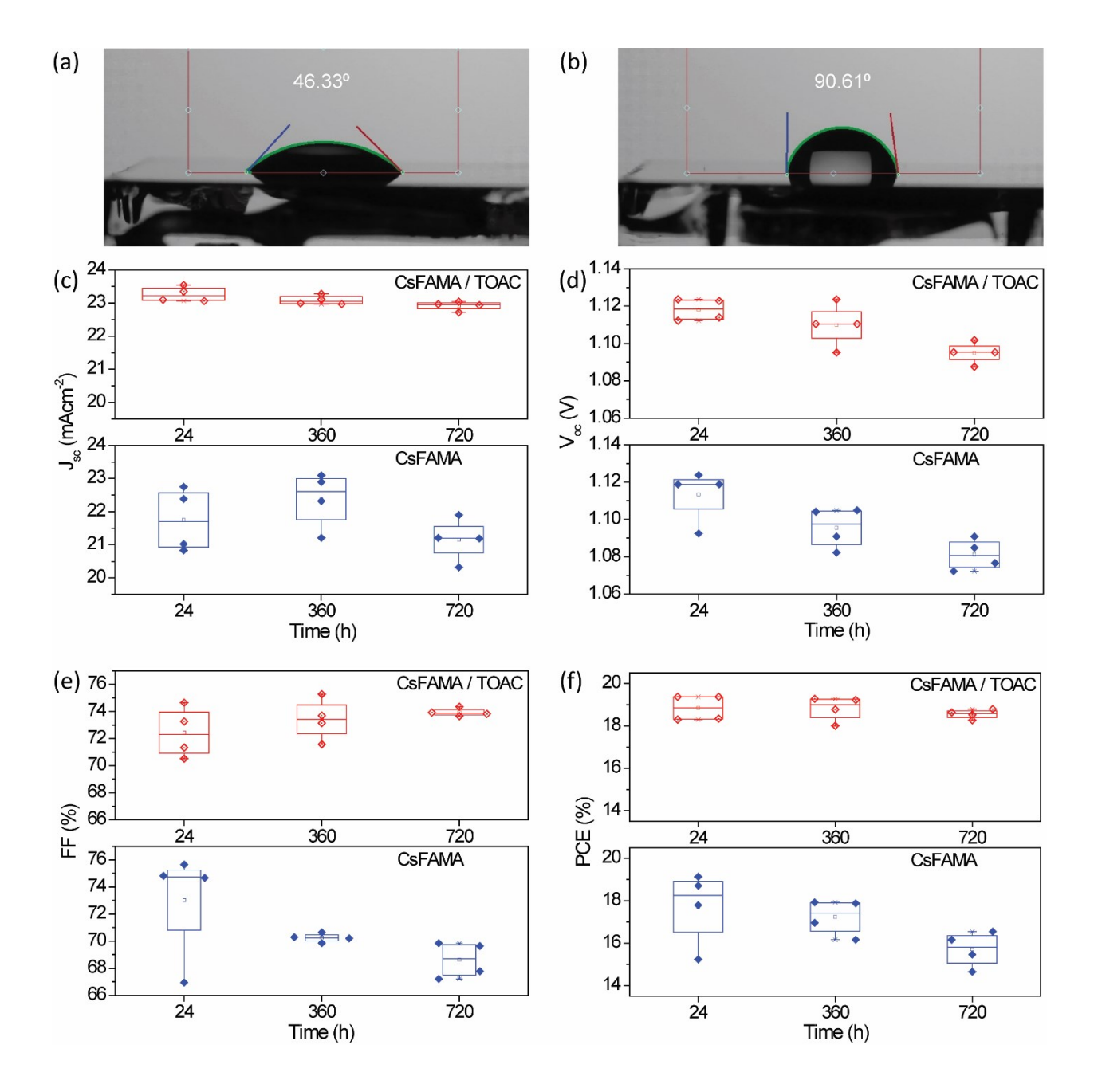


Figure 6. Water contact angle of (a) CsFAMA, (b) CsFAMA/TOAC. Long-term stability of CsFAMA and CsFAMA/ TOAC based device in air (RH= 40-55%) for 720 hours (c)  $J_{sc}$ , (d)  $V_{oc}$ , (e) FF and (f) PCE.

Long-term stability of CsFAMA and CsFAMA /TOAC-based PSCs in air (RH= 40-55%) for 720 hours.

In the next section, we use TOAC to passivate MAPbI<sub>3</sub> Film/devices compared with the control MAPbI<sub>3</sub> to assess the universality of TOAC passivation approach on defect suppression and the stability of solar cells. From device optimization we have observed only a small amount of TOAC (0.5 mM) is required to passivate the MAPbI<sub>3</sub> unlike CsFAMA (2.5 mM). We follow similar approaches and techniques to investigate the MAPbI<sub>3</sub> and MAPbI<sub>3</sub> / TOAC films and devices. FTIR is employed to study the incorporation of TOAC into MAPbI<sub>3</sub>. The FTIR spectra of TOAC, MAPbI<sub>3</sub>, and MAPbI<sub>3</sub> / TOAC are presented in Figure 7a-f. The FTIR peaks at 907 cm<sup>-1</sup> (CH<sub>3</sub>-NH<sub>3</sub><sup>+</sup> rock)<sup>52, 61</sup>, 961 cm<sup>-1</sup> (C-N stretch)<sup>52, 61</sup>, 1247 cm<sup>-1</sup> (CH<sub>3</sub>-NH<sub>3</sub><sup>+</sup> rock)<sup>61</sup>, 1468 cm<sup>-1</sup> (sym. NH<sub>3</sub><sup>+</sup> bend)<sup>61</sup>, 1577 cm<sup>-1</sup> (asym. NH<sub>3</sub><sup>+</sup> bend)<sup>61</sup>, 3133 cm<sup>-1</sup> (sym. NH<sub>3</sub><sup>+</sup> stretch)<sup>52,61</sup> and 3178 cm<sup>-1</sup> (asym. NH<sub>3</sub><sup>+</sup> stretch)<sup>52, 61</sup> of the control MAPbI<sub>3</sub> film are shifted to lower wavenumber of 906 cm<sup>-1</sup>, 959 cm<sup>-1</sup>, 1246 cm<sup>-1</sup>, 1465 cm<sup>-1</sup>, 1575 cm<sup>-1</sup>, 3131 cm<sup>-1</sup> and 3174 cm<sup>-1</sup>, respectively for the modified film. The peak at 2850 cm<sup>-1</sup> (sym. CH<sub>3</sub> rock)<sup>52, 61</sup>, 2918 cm<sup>-1</sup> (sym. CH<sub>3</sub> stretch)<sup>52, 61</sup>, and 2954 cm<sup>-1</sup> (asym. CH<sub>3</sub> stretch)<sup>52, 61</sup> of the TOAC molecule shifted to 2856 cm<sup>-1</sup>, 2926 cm<sup>-1</sup>, and 2957 cm<sup>-1</sup>, respectively for treated MAPbI<sub>3</sub>/TOAC which demonstrated the existence of strong chemical interaction between TOAC and CsFAMA. The shifts of NH<sub>3</sub><sup>+</sup> stretching and NH<sub>3</sub><sup>+</sup> bending to lower wavenumber show that there are strong interactions between TOAC and MAPbI<sub>3</sub> through hydrogen bonding of the NH<sub>3</sub><sup>+</sup> and TOAC (N-H···Cl). <sup>60, 62-64</sup> The full FTIR spectra are presented in Figure S4. We investigate the MAPbI<sub>3</sub>/TOAC film surface composition by EDX elemental mapping, where evenly distributed Cl atoms all over the MAPbI<sub>3</sub> surface are observed (Figure S5). Both FTIR and EDX mapping validated the incorporation of TOAC into the MAPbI<sub>3</sub> film.

Figure 7g showed the XRD of MAPbI<sub>3</sub> and MAPbI<sub>3</sub> / TOAC on FTO. The XRD peak at about 12. 6º belongs to the excess PbI<sub>2</sub> added to enhance the PCE of the device. After passivation, we haven't

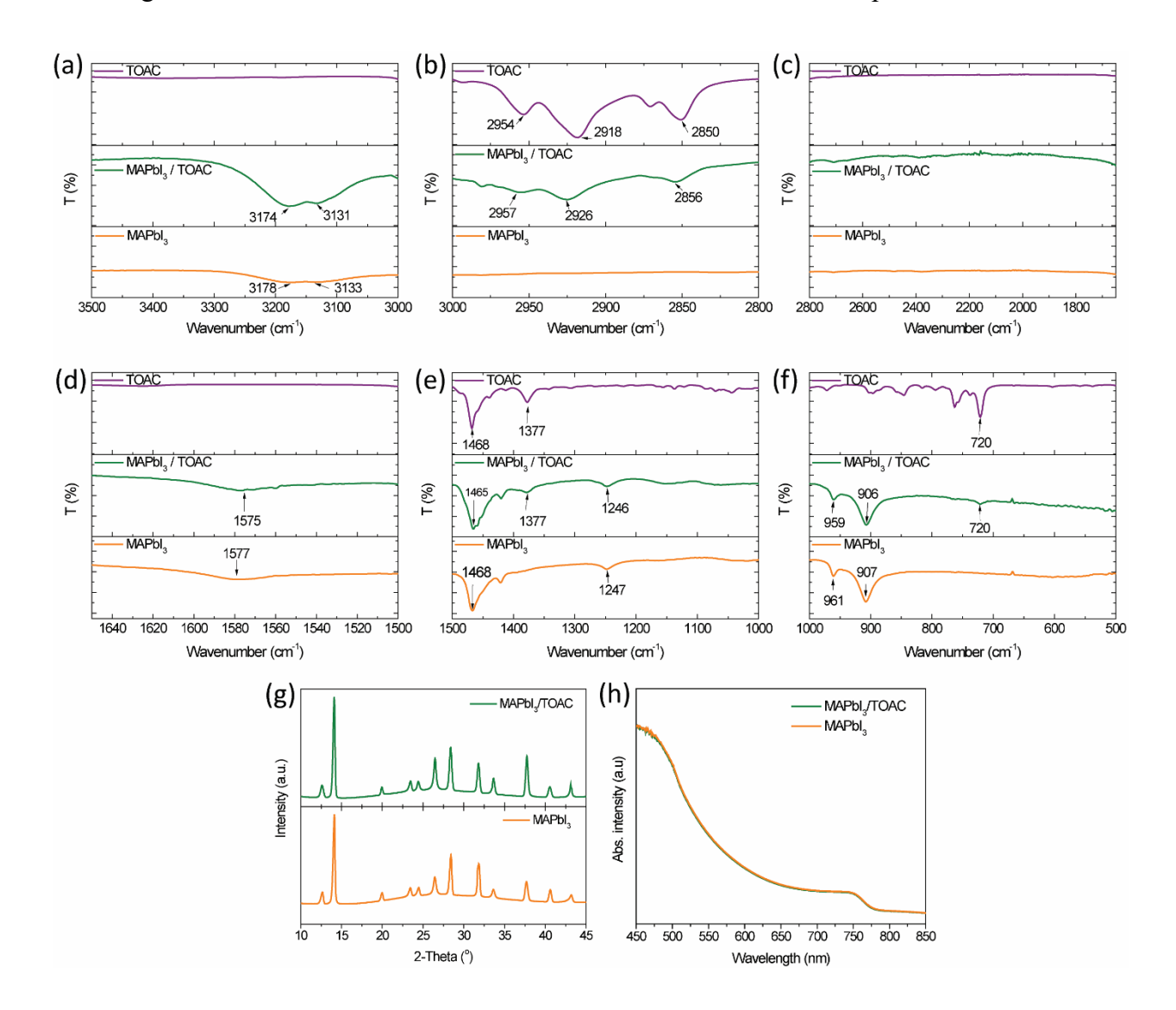


Figure 7. (a-f) FTIR spectra of TOAC, MAPbI<sub>3</sub>, and MAPbI<sub>3</sub>/ TOAC (g) XRD diffraction patterns of MAPbI<sub>3</sub> and MAPbI<sub>3</sub> passivated with 0.5 mM TOAC (h) UV-vis absorption spectra of MAPbI<sub>3</sub> with and without 0.5 mM TOAC.

observed any significant peak position change. This means the crystal property of the perovskite is not influenced by the TOAC. The UV-vis characterization (presented in Figure 7h) of the control

and MAPbI<sub>3</sub> / TOAC has shown similar absorption profiles, where, both films exhibited an absorption onset of *ca.* 775 nm.

Figure 8a and Figure 8b demonstrate the top-view SEM images of MAPbI<sub>3</sub> and MAPbI<sub>3</sub>/ TOAC film. We can barely see any significant difference between the two films. The PbI<sub>2</sub> white grains are equivalently distributed on both surfaces. The cross-sectional SEM of the control MAPbI<sub>3</sub>-based device and the passivated MAPbI<sub>3</sub>-based devices are presented in Figure 8c and Figure 8d, respectively. About 200 nm semi-transparent perovskite thickness is achieved in both layers. The top view AFM, 3-D AFM, and AFM height for MAPbI<sub>3</sub> and CsFAMA / TOAC are presented in Figure 9a-c and Figure 9d-f, respectively. The surface roughness of MAPbI<sub>3</sub> is 16.4 nm and after TOAC passivation the surface roughness decreases slightly to 15.3 nm. The AFM height images of MAPbI<sub>3</sub> and MAPbI<sub>3</sub>/TOAC across 5 μm film in two sections are collected. The TOAC passivation slightly improves the MAPbI<sub>3</sub> smoothness. As the optimized TOAC concentration is small (optimized with respect to device performance), the passivation does not influence morphology and surface roughness significantly.

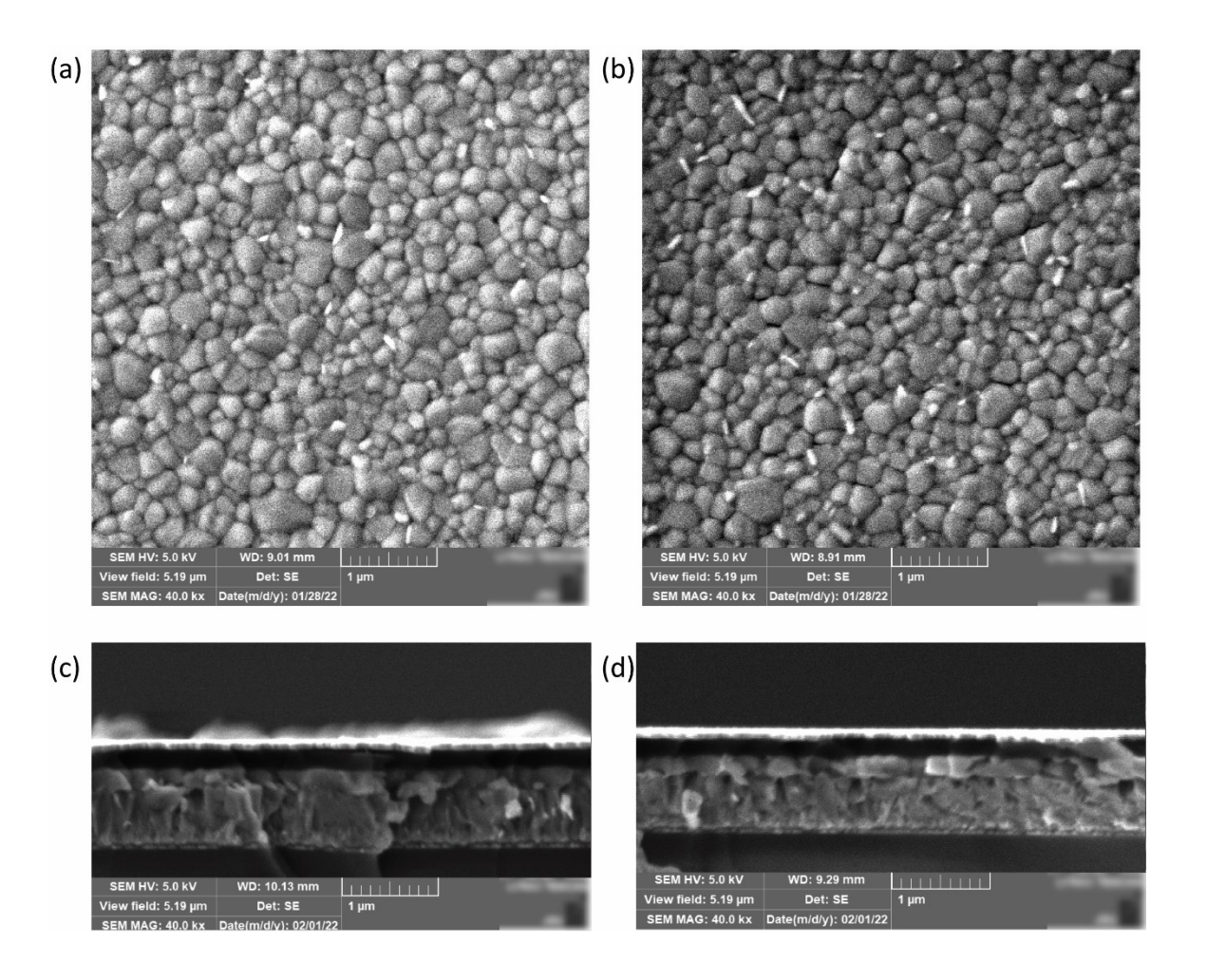


Figure 8. Top-view SEM images of (a) MAPbI<sub>3</sub>, and (b) MAPbI<sub>3</sub>/ 0.5mM TAOC. (c) Cross-sectional SEM image of FTO/SnO<sub>2</sub>/MAPbI<sub>3</sub>/Spiro-OMeTAD/Au, and (d) Cross-sectional SEM image of FTO/SnO<sub>2</sub>/MAPbI<sub>3</sub>/TOAC/Spiro-OMeTAD/Au.

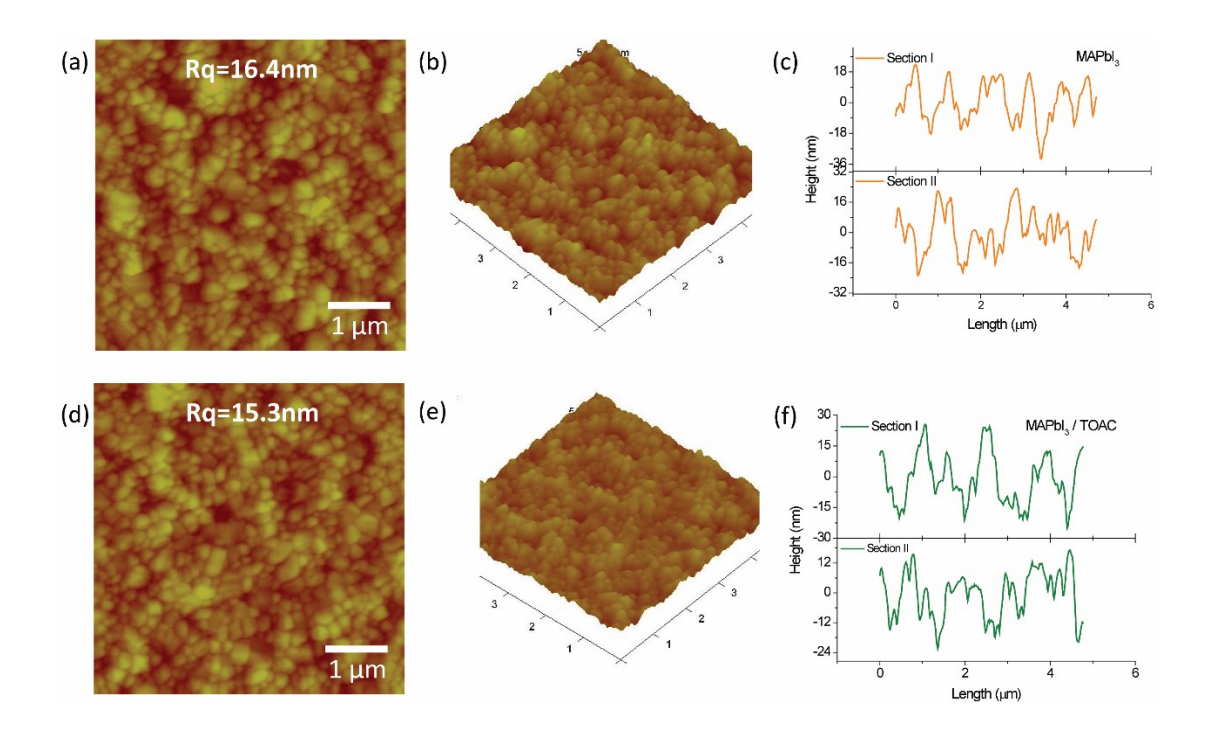


Figure 9. (a-c) AFM surface image, 3-dimensional image, and height image for MAPbI<sub>3</sub>, respectively. (d-f) AFM surface image, 3-dimensional image, and height image for MAPbI<sub>3</sub> / TOAC, respectively.

Figure 10 (a) shows the steady-state PL spectra of MAPbI<sub>3</sub>, MAPbI<sub>3</sub> / TOAC, MAPbI<sub>3</sub> / Spiro-OMeTAD and MAPbI<sub>3</sub> / TOAC / Spiro-OMeTAD. The perovskite films are spun at a glass substrate and the incident light is guided from the perovskite side to collect the spectra. The PL study strikingly reveals that the MAPbI<sub>3</sub> / TOAC film exhibits improved photoluminescence (~ 50% raise on PL intensity) compared to the control MAPbI<sub>3</sub>. This suggests the TOAC could passivate defects at the surface and grain boundaries of the MAPbI<sub>3</sub> film which is consistent with the phenomenon we observed for CsFAMA film. The TOAC plays a crucial role in both the mixed and MAPbI<sub>3</sub> perovskite by suppressing surface defects and enhancing photoluminescence. The charge extraction property of the films is studied by deposit spiro-OMeTAD on control MAPbI<sub>3</sub> and MAPbI<sub>3</sub> / TOAC layers. Both films demonstrate PL quenching. The control MAPbI<sub>3</sub> / spiro-

OMeTAD quenches 68% vs 87% PL quenching for MAPbI<sub>3</sub>/TOAC /Spiro-OMeTAD. This result proves the remarkable potential of TOAC to impede the nonradiative recombination; eliminate traps on the surface and grain boundaries; facilitate charge extractions, and enhance photoluminescence. Such properties are needed to achieve high-performance PSCs. Figure 10b shows the TRPL spectra of the control and passivated MAPbI<sub>3</sub> films. Equation (1) equation (2) are employed to fit the lifetime and to calculate the average lifetimes of the films. The average lifetime of the control MAPbI<sub>3</sub> is 80.31 ns. After TOAC passivation, the lifetime MAPbI<sub>3</sub> / TOAC increased more than three-fold to 298.93 ns. The longer lifetime of the passivated MAPBI<sub>3</sub> suggests that there is a significant suppression of defects on the surface and grain boundaries of MAPbI<sub>3</sub> by TOAC treatment. The lifetime of MAPbI<sub>3</sub>/ Spiro-OMeTAD is 43.57ns vs 30.28ns for MAPbI<sub>3</sub>/TOAC/Spiro-OMeTAD which demonstrates the charge extraction of MAPbI<sub>3</sub> enhanced after TOAC passivation. These results are consistent with the PL studies. The lifetime result of MAPbI<sub>3</sub> and MAPbI<sub>3</sub>/ TOAC are summarized in Table S6.

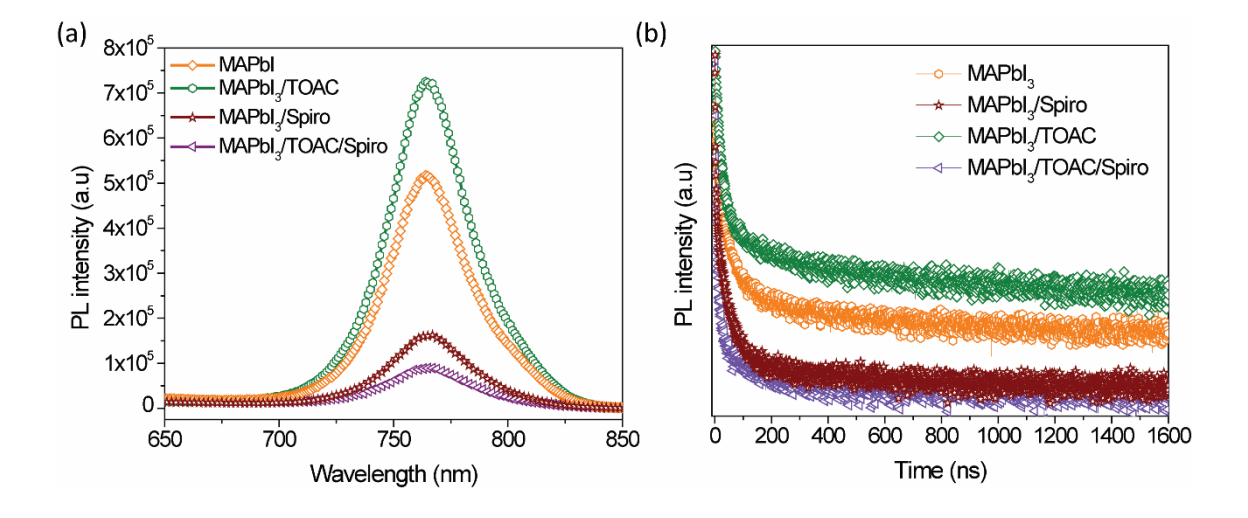


Figure 10. (a) Steady state PL spectra and (b) TRPL spectra of MAPbI<sub>3</sub>, MAPbI<sub>3</sub>/Spiro-OMeTAD, MAPbI<sub>3</sub>/TOAC and MAPbI<sub>3</sub>/TOAC/Spiro-OMeTAD.

To test the influence of TOAC on the performance of MAPbI<sub>3</sub>-based devices, solar cells with a structure of FTO/SnO<sub>2</sub>/MAPbI<sub>3</sub> (with and without TOAC)/ spiro-OMeTAD/Au are fabricated. Various concentrations of TOAC (0.5mM, 1mM and 1.5mM) treatment are investigated and optimized (Figure 11a-d). We observe MAPbI<sub>3</sub> required only a very dilute concentration of TOAC (0.5 mM) to exhibit the optimized PCE compared to the CsFAMA film (2.5 mM). The standard device exhibits a maximum PCE of 18.07% with a J<sub>sc</sub> of 21.70 mAcm<sup>-2</sup>, V<sub>oc</sub> of 1.07 V, FF of 77.90 %. Expectedly, the 0.5 mM TOAC passivated MAPbI<sub>3</sub> exhibits the champion performance of 19.27% PCE with a J<sub>sc</sub> of 22.25 mAcm<sup>-2</sup>, Voc of 1.09 V, and FF 79.27% (Figure 11e and Table S7). When the concentration of TOAC increases to 1 mM and 1.5 mM the current density of the passivated devices deteriorated. The stabilized power output of the champion MAPbI<sub>3</sub> and MAPbI<sub>3</sub> / TOAC based devices are presented in Figure S6. To get a clear picture of the charge recombination process on the control and passivated device we carry out EIS measurement at dark at a bias of 0.9 V. The EIS curve and the equivalent circuit are presented in Figure 11f and summarized in Table S8. The fitting results display that the contact capacitance of the control MAPbI<sub>3</sub> with adjust layer is two orders higher than the TOAC passivated layer, which means the control device suffers from charge buildup at the interface that is a source of non-radiative charge recombination, photoluminescence loss, and device instability.<sup>9, 70</sup> The R<sub>rec</sub> of the passivated device showed a two-fold increment to 4236  $\Omega$  compared to the control device (2181  $\Omega$ ). This demonstrates the TOAC passivation suppresses defects on the surface and grain boundaries.

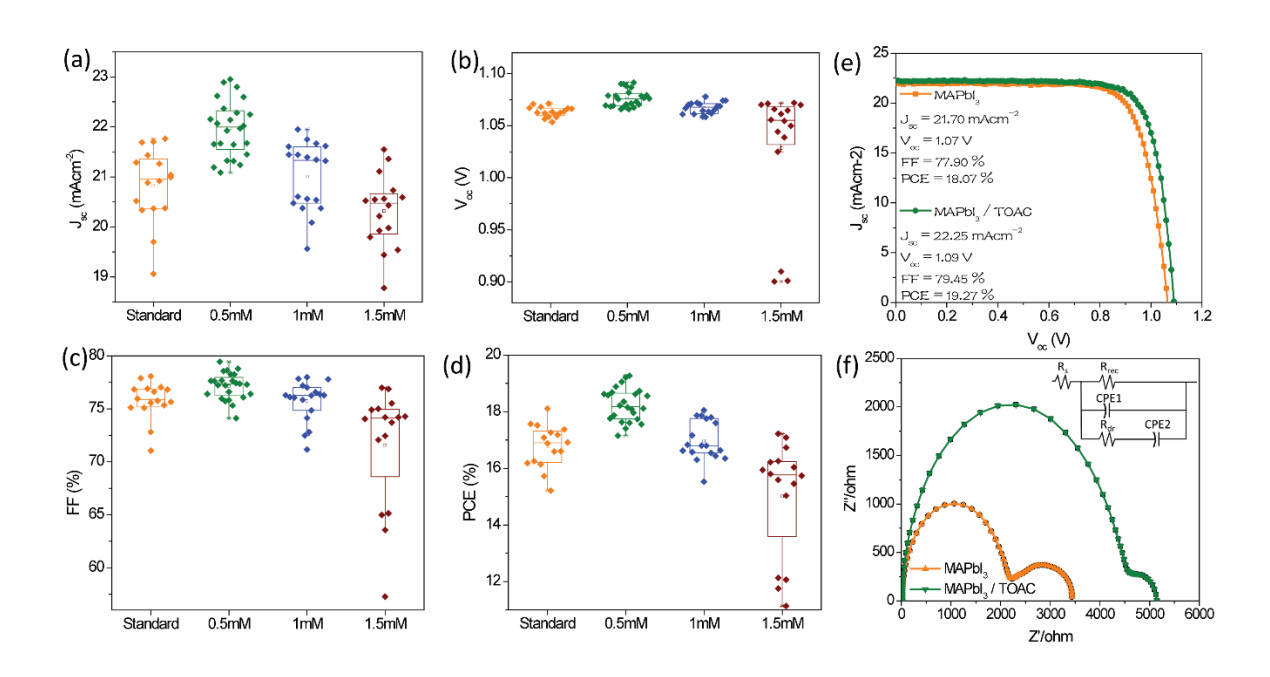


Figure 11. (a) Box chart of the J-V parameters for the standard MAPbI<sub>3</sub> and various concentrations TOAC passivated MAPbI<sub>3</sub> (a) Jsc, (b) Voc, (c) FF, and (d) PCE. (e) Champion J-V curve for the standard and 0.5mM TOAC passivated MAPbI<sub>3</sub> device (f) Nyquist plots of the devices without and with 0.5 mM passivated MAPbI<sub>3</sub>

The trap state density of MAPbI<sub>3</sub> and MAPbI<sub>3</sub> / TOAC-based devices are investigated by fabricating FTO/SnO<sub>2</sub>/ MAPbI<sub>3</sub> (with and without TOAC)/PCBM/Au to calculate the number of electron traps, and a structure of FTO/PTAA/ MAPbI<sub>3</sub> (with and without TOAC)/Spiro-OMeTAD/Au to calculate the number of hole traps (Figure 12a-b). The N<sub>traps</sub> for the respective devices is calculated following equation (3), where, the relative dielectric constant (ε) of 32 was adopted for CH<sub>3</sub>NH<sub>3</sub>PbI<sub>3</sub>.<sup>67</sup> The N<sub>traps</sub> for the control electron-only device is 8.10×10<sup>16</sup>cm<sup>-3</sup>, and with TOAC passivation the electron traps are significantly reduced to 5.77×10<sup>16</sup> cm<sup>-3</sup>. However, for the control hole-only device the N<sub>traps</sub> was 2.42×10<sup>16</sup> cm<sup>-3</sup>, and after passivation, the N<sub>traps</sub> traps decreases to 1.95×10<sup>16</sup> cm<sup>-3</sup>. From this, we can conclude that TOAC could passivate more electron traps than the hole traps. This trend is consistent with the N<sub>traps</sub> calculated for CsFAMA with and

without passivation. The SCLC parameters of MAPbI<sub>3</sub> and MAPbI<sub>3</sub> / TOAC are summarized in Table S9.

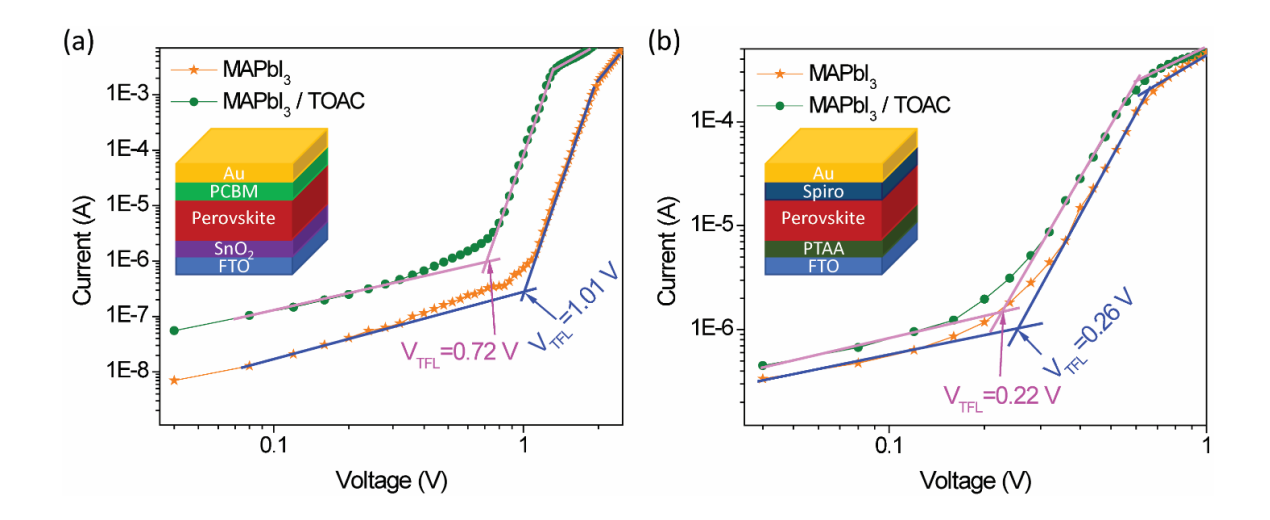


Figure 12. (a) Electron-only device with a structure of FTO/SnO<sub>2</sub>/ MAPbI<sub>3</sub> (with and without 0.5 mM TOAC) /PCBM/Au. (b) Hole-only device with a structure of FTO/PTAA/ MAPbI<sub>3</sub> (with and without 0.5 mM TOAC) /Spiro-OMeTAD/Au

Finally, we investigate the long-term stability of MAPbI<sub>3</sub> and MAPbI<sub>3</sub> / TOAC based devices in the air. Figure 13 a and b show the water contact angles of the MAPbI<sub>3</sub> and MAPbI<sub>3</sub>/TOAC films. The water contact angle values are 49.26° and 81.87° for MAPbI<sub>3</sub> and MAPbI<sub>3</sub>/TOAC films, respectively. This indicates the improved moisture stability of the films caused by the passivation. The devices are kept in the air at (RH = 40-55%) for 720 hours and taken out only for measurement. To have tangible stability information at least five devices of the control and TOAC passivated MAPbI<sub>3</sub> devices are studied, and the results are summarized in Figure 13c-f. The TOAC passivated devices show incredible moisture stability compared to the control device. The control MAPbI<sub>3</sub> retain only an average of 81.70% of their initial PCE. Strikingly, the passivated devices do not show any sign of degradation after 720 h, even some of the devices show PCE improvement

(comes from the increase in FF over time). This demonstrates the potential of TOAC passivation not only to improve the PCE but also to extend the long-term stability of the device.

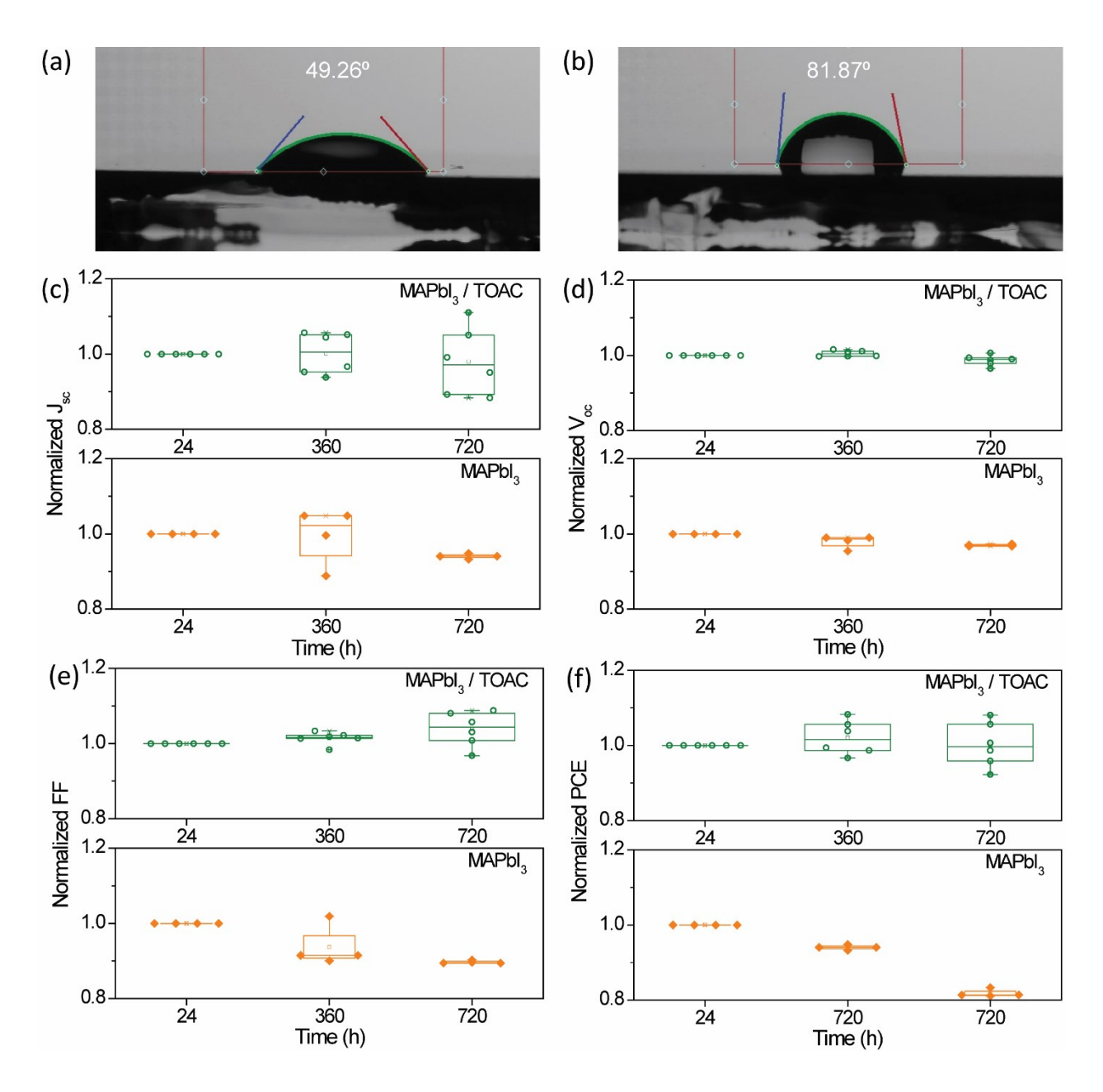


Figure 13. Water contact angle of (a) MAPbI<sub>3</sub>, (b) MAPbI<sub>3</sub>/TOAC. Long-term stability of MAPbI<sub>3</sub> and MAPbI<sub>3</sub>/ TOAC based device in air (RH= 40-55%) for 720 hours (c) normalized  $J_{sc}$ , (d) normalized  $V_{oc}$ , (e) normalized FF and (f) normalized PCE.

# **Conclusions**

In summary, we have successfully developed a universal post-surface treatment strategy to suppress the non-radiative recombination for the widely fabricated mixed perovskite with a composition of Cs<sub>0.05</sub>(FA<sub>0.83</sub>MA<sub>0.17</sub>)<sub>0.95</sub>Pb(I<sub>0.83</sub>Br<sub>0.17</sub>)<sub>3</sub> and MAPbI<sub>3</sub> with TOAC. Various concentrations of TOAC post-treatment could significantly passivate the defects on the surface and grain boundaries of the respective perovskites. TOAC treatment could passivate both electron and hole traps. However, more electron traps passivated than the hole traps. As a result, the charge recombination resistance, photoluminescence, and charge extraction of the passivated films increase substantially. Consequently, the device parameters show significant improvement, and the maximum PCE of 21.24% for Cs<sub>0.05</sub>(FA<sub>0.83</sub>MA<sub>0.17</sub>)<sub>0.95</sub>Pb(I<sub>0.83</sub>Br<sub>0.17</sub>)<sub>3</sub>, and 19.27% for MAPbI<sub>3</sub> is achieved based on our TOAC post-treatment strategy. TOAC not only improves the performance of the cells but also extends the stability of perovskite solar cells. Remarkably, TOAC passivated devices do not show any sign of degradation after 720 h in air.

#### **Associated Content**

#### **Supporting Information**

Full FTIR spectra for all the control and passivated perovskite films, EDX elemental mapping and TRPL calculations for all layers, Box-charts and tables of photovoltaic parameter, EIS fitting calculations, and summarized table for SCLC calculations for all devices.

## Acknowledgment

This material is based on work supported by the National Science Foundation (NSF) under Grant No. 1757220. The steady-state PL and TRPL equipment used in this work is supported by National Science Foundation Research Initiation Award: Novel Perovskite Solar Cells Based on Interface Manipulation (Award#1900047). Q Zhang is supported by NSF-PREM grant #DMR-1826886.

#### References

- 1. Min, H.; Lee, D. Y.; Kim, J.; Kim, G.; Lee, K. S.; Kim, J.; Paik, M. J.; Kim, Y. K.; Kim, K. S.; Kim, M. G.; Shin, T. J.; Il Seok, S. Perovskite Solar Cells with Atomically Coherent Interlayers on SnO2 Electrodes. *Nature* **2021**, *598* (7881), 444-450.
- 2. Jeong, J.; Kim, M.; Seo, J.; Lu, H.; Ahlawat, P.; Mishra, A.; Yang, Y.; Hope, M. A.; Eickemeyer, F. T.; Kim, M.; Yoon, Y. J.; Choi, I. W.; Darwich, B. P.; Choi, S. J.; Jo, Y.; Lee, J. H.; Walker, B.; Zakeeruddin, S. M.; Emsley, L.; Rothlisberger, U.; Hagfeldt, A.; Kim, D. S.; Gratzel, M.; Kim, J. Y. Pseudo-Halide Anion Engineering for Alpha-FAPbI3 Perovskite Solar Cells. *Nature* **2021**, *592* (7854), 381-385.
- 3. Wang, F.; Yang, M.; Yang, S.; Qu, X.; Yang, L.; Fan, L.; Yang, J.; Rosei, F. Iodine-Assisted Antisolvent Engineering for Stable Perovskite Solar Cells with Efficiency >21.3 %. *Nano Energy* **2020**, *67*, 104224.
- 4. Aydin, E.; De Bastiani, M.; De Wolf, S. Defect and Contact Passivation for Perovskite Solar Cells. *Adv. Mater.* **2019**, *31* (25), e1900428.
- 5. Qiu, X.; Liu, Y.; Li, W.; Hu, Y. Traps in Metal Halide Perovskites: Characterization and Passivation. *Nanoscale* **2020**, *12* (44), 22425-22451.
- 6. Li, X.; Dar, M. I.; Yi, C.; Luo, J.; Tschumi, M.; Zakeeruddin, S. M.; Nazeeruddin, M. K.; Han, H.; Gratzel, M. Improved Performance and Stability of Perovskite Solar Cells by Crystal Crosslinking with Alkylphosphonic Acid Omega-Ammonium Chlorides. *Nat. Chem.* **2015**, *7* (9), 703-11.
- 7. Fu, L.; Li, H.; Wang, L.; Yin, R.; Li, B.; Yin, L. Defect Passivation Strategies in Perovskites for an Enhanced Photovoltaic Performance. *Energy Environ. Sci.* **2020**, *13* (11), 4017-4056.

- 8. Chen, B.; Rudd, P. N.; Yang, S.; Yuan, Y.; Huang, J. Imperfections and Their Passivation in Halide Perovskite Solar Cells. *Chem. Soc. Rev.* **2019**, *48* (14), 3842-3867.
- 9. Byranvand, M. M.; Saliba, M. Defect Passivation of Perovskite Films for Highly Efficient and Stable Solar Cells. *Sol. RRL* **2021**, *5* (8), 2100295
- 10. Mohd Yusoff, A. R. b.; Vasilopoulou, M.; Georgiadou, D. G.; Palilis, L. C.; Abate, A.; Nazeeruddin, M. K. Passivation and Process Engineering Approaches of Halide Perovskite Films for High Efficiency and Stability Perovskite Solar Cells. *Energy Environ. Sci.* **2021**, *14* (5), 2906-2953.
- 11. Duan, C.; Cui, J.; Zhang, M.; Han, Y.; Yang, S.; Zhao, H.; Bian, H.; Yao, J.; Zhao, K.; Liu, Z.; Liu, S. Precursor Engineering for Ambient-Compatible Antisolvent-Free Fabrication of High-Efficiency CsPbI2Br Perovskite Solar Cells. *Adv. Energy Mater.* **2020**, *10* (22), 2000691.
- 12. Zhao, H.; Xu, Z.; Che, Y.; Han, Y.; Yang, S.; Duan, C.; Cui, J.; Dai, S.; Liu, Z.; Liu, S. Simultaneous Dual-Interface and Bulk Defect Passivation for High-Efficiency and Stable CsPbI2Br Perovskite Solar Cells. *J. Power Sources* **2021**, *492*, 229580.
- 13. Zhou, X.; Hu, M.; Liu, C.; Zhang, L.; Zhong, X.; Li, X.; Tian, Y.; Cheng, C.; Xu, B. Synergistic Effects of Multiple Functional Ionic Liquid-Treated PEDOT:PSS and Less-Ion-Defects S-Acetylthiocholine Chloride-Passivated Perovskite Surface Enabling Stable and Hysteresis-Free Inverted Perovskite Solar Cells with Conversion Efficiency Over 20%. *Nano Energy* **2019**, *63*, 103866.
- 14. Liu, P.; Wang, W.; Liu, S.; Yang, H.; Shao, Z. Fundamental Understanding of Photocurrent Hysteresis in Perovskite Solar Cells. *Adv. Energy Mater.* **2019**, *9* (13), 1803017

- 15. Shao, Y.; Xiao, Z.; Bi, C.; Yuan, Y.; Huang, J. Origin and Elimination of Photocurrent Hysteresis by Fullerene Passivation in CH3NH3PbI3 Planar Heterojunction Solar Cells. *Nat. Commun.* **2014**, *5* (1), 5784.
- 16. Son, D. Y.; Kim, S. G.; Seo, J. Y.; Lee, S. H.; Shin, H.; Lee, D.; Park, N. G. Universal Approach Toward Hysteresis-Free Perovskite Solar Cell via Defect Engineering. *J. Am. Chem. Soc.* **2018**, *140* (4), 1358-1364.
- 17. Gao, F.; Zhao, Y.; Zhang, X.; You, J. Recent Progresses on Defect Passivation Toward Efficient Perovskite Solar Cells. *Adv. Energy Mater.* **2019**, *10* (13), 1902650.
- 18. Wu, W.-Q.; Yang, Z.; Rudd, P. N.; Shao, Y.; Dai, X.; Wei, H.; Zhao, J.; Fang, Y.; Wang, Q.; Liu, Y.; Deng, Y.; Xiao, X.; Feng, Y.; Huang, J. Bilateral Alkylamine for Suppressing Charge Recombination and Improving Stability in Blade-Coated Perovskite Solar Cells. *Sci. Adv.* **2019**, *5* (3), eaav8925
- 19. Lee, J.-W.; Bae, S.-H.; Hsieh, Y.-T.; De Marco, N.; Wang, M.; Sun, P.; Yang, Y. A Bifunctional Lewis Base Additive for Microscopic Homogeneity in Perovskite Solar Cells. *Chem* **2017**, *3* (2), 290-302.
- 20. Li, H.; Tao, L.; Huang, F.; Sun, Q.; Zhao, X.; Han, J.; Shen, Y.; Wang, M. Enhancing Efficiency of Perovskite Solar Cells via Surface Passivation with Graphene Oxide Interlayer. *ACS Appl. Mater. Interfaces* **2017**, *9* (44), 38967-38976.
- 21. Wu, Z.; Jiang, M.; Liu, Z.; Jamshaid, A.; Ono, L. K.; Qi, Y. Highly Efficient Perovskite Solar Cells Enabled by Multiple Ligand Passivation. *Adv. Energy Mater.* **2020**, *10* (10), 1903696.
- 22. Jiang, Q.; Zhao, Y.; Zhang, X.; Yang, X.; Chen, Y.; Chu, Z.; Ye, Q.; Li, X.; Yin, Z.; You, J. Surface Passivation of Perovskite Film for Efficient Solar Cells. *Nat. Photonics* **2019**, *13* (7), 460-466.

- 23. Luo, W.; Wu, C.; Wang, D.; Zhang, Y.; Zhang, Z.; Qi, X.; Zhu, N.; Guo, X.; Qu, B.; Xiao, L.; Chen, Z. Efficient and Stable Perovskite Solar Cell with High Open-Circuit Voltage by Dimensional Interface Modification. *ACS Appl. Mater. Interfaces* **2019**, *11* (9), 9149-9155.
- 24. Poorkazem, K.; Kelly, Timothy L. Improving the Stability and Decreasing the Trap State Density of Mixed-Cation Perovskite Solar Cells through Compositional Engineering. *Sustain. Energy Fuels* **2018**, *2* (6), 1332-1341.
- 25. Zhao, T.; Chueh, C.-C.; Chen, Q.; Rajagopal, A.; Jen, A. K. Y. Defect Passivation of Organic–Inorganic Hybrid Perovskites by Diammonium Iodide toward High-Performance Photovoltaic Devices. *ACS Energy Lett.* **2016**, *1* (4), 757-763.
- 26. De Marco, N.; Zhou, H.; Chen, Q.; Sun, P.; Liu, Z.; Meng, L.; Yao, E. P.; Liu, Y.; Schiffer, A.; Yang, Y. Guanidinium: A Route to Enhanced Carrier Lifetime and Open-Circuit Voltage in Hybrid Perovskite Solar Cells. *Nano Lett.* **2016**, *16* (2), 1009-16.
- 27. Khadka, D. B.; Shirai, Y.; Yanagida, M.; Masuda, T.; Miyano, K. Enhancement in Efficiency and Optoelectronic Quality of Perovskite Thin Films Annealed in MACl Vapor. *Sustain. Energy Fuels* **2017**, *1* (4), 755-766.
- 28. Uribe, J. I.; Ciro, J.; Montoya, J. F.; Osorio, J.; Jaramillo, F. Enhancement of Morphological and Optoelectronic Properties of Perovskite Films by CH3NH3Cl Treatment for Efficient Solar Minimodules. *ACS Appl. Energy Mater.* **2018**, *1* (3), 1047-1052.
- 29. Kim, M.; Kim, G.-H.; Lee, T. K.; Choi, I. W.; Choi, H. W.; Jo, Y.; Yoon, Y. J.; Kim, J. W.; Lee, J.; Huh, D.; Lee, H.; Kwak, S. K.; Kim, J. Y.; Kim, D. S. Methylammonium Chloride Induces Intermediate Phase Stabilization for Efficient Perovskite Solar Cells. *Joule* **2019**, *3* (9), 2179-2192.

- 30. Zheng, X.; Yuan, S.; Liu, J.; Yin, J.; Yuan, F.; Shen, W.-S.; Yao, K.; Wei, M.; Zhou, C.; Song, K.; Zhang, B.-B.; Lin, Y.; Hedhili, M. N.; Wehbe, N.; Han, Y.; Sun, H.-T.; Lu, Z.-H.; Anthopoulos, T. D.; Mohammed, O. F.; Sargent, E. H.; Liao, L.-S.; Bakr, O. M. Chlorine Vacancy Passivation in Mixed Halide Perovskite Quantum Dots by Organic Pseudohalides Enables Efficient Rec. 2020 Blue Light-Emitting Diodes. *ACS Energy Lett.* **2020**, *5* (3), 793-798.
- 31. Oliver, R. D. J.; Lin, Y.-H.; Horn, A. J.; Xia, C. Q.; Warby, J. H.; Johnston, M. B.; Ramadan, A. J.; Snaith, H. J. Thermally Stable Passivation toward High Efficiency Inverted Perovskite Solar Cells. *ACS Energy Lett.* **2020**, *5* (11), 3336-3343.
- 32. Li, Y.; Wu, H.; Qi, W.; Zhou, X.; Li, J.; Cheng, J.; Zhao, Y.; Li, Y.; Zhang, X. Passivation of Defects in Perovskite Solar Cell: From a Chemistry Point of View. *Nano Energy* **2020**, *77*, 105237.
- 33. Liu, W.; Xiong, J.; Liu, N.; Dai, J.; Dai, Z.; Huang, Y.; Zhang, Z.; Xue, X.; Dai, Q.; Zhang, J. Defect Passivation and Interface Modification by Tetra-n-octadecyl Ammonium Bromide for Efficient and Stable Inverted Perovskite Solar Cells. *Chem. Eng. J.* **2022**, *429*, 132426.
- 34. Lin, Y.; Bai, Y.; Fang, Y.; Chen, Z.; Yang, S.; Zheng, X.; Tang, S.; Liu, Y.; Zhao, J.; Huang, J. Enhanced Thermal Stability in Perovskite Solar Cells by Assembling 2D/3D Stacking Structures. *J. Phys. Chem. Lett.* **2018**, *9* (3), 654-658.
- 35. Stoddard, R. J.; Rajagopal, A.; Palmer, R. L.; Braly, I. L.; Jen, A. K. Y.; Hillhouse, H. W. Enhancing Defect Tolerance and Phase Stability of High-Bandgap Perovskites via Guanidinium Alloying. *ACS Energy Lett.* **2018**, *3* (6), 1261-1268.
- 36. Jung, E. H.; Jeon, N. J.; Park, E. Y.; Moon, C. S.; Shin, T. J.; Yang, T. Y.; Noh, J. H.; Seo, J. Efficient, Stable and Scalable Perovskite Solar Cells using Poly(3-hexylthiophene). *Nature* **2019**, *567* (7749), 511-515.

- 37. Yao, Q.; Xue, Q.; Li, Z.; Zhang, K.; Zhang, T.; Li, N.; Yang, S.; Brabec, C. J.; Yip, H. L.; Cao, Y. Graded 2D/3D Perovskite Heterostructure for Efficient and Operationally Stable MA-Free Perovskite Solar Cells. *Adv Mater* **2020**, *32* (26), e2000571.
- 38. Zheng, X.; Chen, B.; Dai, J.; Fang, Y.; Bai, Y.; Lin, Y.; Wei, H.; Zeng, Xiao C.; Huang, J. Defect Passivation in Hybrid Perovskite Solar Cells Using Quaternary Ammonium Halide Anions and Cations. *Nat. Energy* **2017**, *2* (7), 1-9.
- 39. Son, D.-Y.; Lee, J.-W.; Choi, Y. J.; Jang, I.-H.; Lee, S.; Yoo, P. J.; Shin, H.; Ahn, N.; Choi, M.; Kim, D.; Park, N.-G. Self-Formed Grain Boundary Healing Layer for Highly Efficient CH3NH3PbI3 Perovskite Solar Cells. *Nat. Energy* **2016**, *I* (7), 1-8.
- 40. Poli, I.; Eslava, S.; Cameron, P. Tetrabutylammonium Cations for Moisture-Resistant and Semitransparent Perovskite Solar Cells. *J. Mater. Chem. A* **2017**, *5* (42), 22325-22333.
- 41. Liu, Y.; Akin, S.; Pan, L.; Uchida, R.; Arora, N.; Milić, J. V.; Hinderhofer, A.; Schreiber, F.; Uhl, A. R.; Zakeeruddin, S. M.; Hagfeldt, A.; Dar, M. I.; Grätzel, M. Ultrahydrophobic 3D/2D Fluoroarene Bilayer-Based Water-Resistant Perovskite Solar Cells with Efficiencies Exceeding 22%. *Sci. Adv.* **2019**, *5* (6), No. eaaw2543.
- 42. Hawash, Z.; Raga, S. R.; Son, D. Y.; Ono, L. K.; Park, N. G.; Qi, Y. Interfacial Modification of Perovskite Solar Cells Using an Ultrathin MAI Layer Leads to Enhanced Energy Level Alignment, Efficiencies, and Reproducibility. *J. Phys. Chem. Lett.* **2017**, *8* (17), 3947-3953.
- 43. Kubicki, D. J.; Prochowicz, D.; Hofstetter, A.; Saski, M.; Yadav, P.; Bi, D.; Pellet, N.; Lewinski, J.; Zakeeruddin, S. M.; Gratzel, M.; Emsley, L. Formation of Stable Mixed Guanidinium-Methylammonium Phases with Exceptionally Long Carrier Lifetimes for High-Efficiency Lead Iodide-Based Perovskite Photovoltaics. *J. Am. Chem. Soc.* **2018**, *140* (9), 3345-3351.

- 44. Alharbi, E. A.; Alyamani, A. Y.; Kubicki, D. J.; Uhl, A. R.; Walder, B. J.; Alanazi, A. Q.; Luo, J.; Burgos-Caminal, A.; Albadri, A.; Albrithen, H.; Alotaibi, M. H.; Moser, J. E.; Zakeeruddin, S. M.; Giordano, F.; Emsley, L.; Gratzel, M. Atomic-Level Passivation Mechanism of Ammonium Salts Enabling Highly Efficient Perovskite Solar Cells. *Nat. Commun.* **2019**, *10* (1), 3008.
- Jiang, X.; Chen, S.; Li, Y.; Zhang, L.; Shen, N.; Zhang, G.; Du, J.; Fu, N.; Xu, B. Direct Surface Passivation of Perovskite Film by 4-Fluorophenethylammonium Iodide Toward Stable and Efficient Perovskite Solar Cells. *ACS Appl. Mater. Interfaces* **2021**, *13* (2), 2558-2565.

  46. Wang, Y.; Xu, H.; Wang, F.; Liu, D.; Chen, H.; Zheng, H.; Ji, L.; Zhang, P.; Zhang, T.; Chen, Z. D.; Wu, J.; Chen, L.; Li, S. Unveiling the Guest Effect of N-butylammonium Iodide Towards Efficient and Stable 2D-3D Perovskite Solar Cells Through Sequential Deposition Process. *Chem. Eng. J.* **2020**, *391*, 123589.
- 47. Yang, B.; Suo, J.; Di Giacomo, F.; Olthof, S.; Bogachuk, D.; Kim, Y.; Sun, X.; Wagner, L.; Fu, F.; Zakeeruddin, S. M.; Hinsch, A.; Gratzel, M.; Di Carlo, A.; Hagfeldt, A. Interfacial Passivation Engineering of Perovskite Solar Cells with Fill Factor over 82% and Outstanding Operational Stability on n-i-p Architecture. *ACS Energy Lett.* **2021**, *6* (11), 3916-3923.
- 48. Yang, B.; Suo, J.; Mosconi, E.; Ricciarelli, D.; Tress, W.; De Angelis, F.; Kim, H.-S.; Hagfeldt, A. Outstanding Passivation Effect by a Mixed-Salt Interlayer with Internal Interactions in Perovskite Solar Cells. *ACS Energy Lett.* **2020**, *5* (10), 3159-3167.
- 49. Zhuang, J.; Mao, P.; Luan, Y.; Yi, X.; Tu, Z.; Zhang, Y.; Yi, Y.; Wei, Y.; Chen, N.; Lin, T.; Wang, F.; Li, C.; Wang, J. Interfacial Passivation for Perovskite Solar Cells: The Effects of the Functional Group in Phenethylammonium Iodide. *ACS Energy Lett.* **2019**, *4* (12), 2913-2921.

- 50. Hauschild, D.; Seitz, L.; Gharibzadeh, S.; Steininger, R.; Jiang, N.; Yang, W.; Paetzold, U. W.; Heske, C.; Weinhardt, L. Impact of n-Butylammonium Bromide on the Chemical and Electronic Structure of Double-Cation Perovskite Thin Films. *ACS Appl. Mater. Interfaces* **2021**, (13), 53202–53210.
- 51. Krishna, A.; Akhavan Kazemi, M. A.; Sliwa, M.; Reddy, G. N. M.; Delevoye, L.; Lafon, O.; Felten, A.; Do, M. T.; Gottis, S.; Sauvage, F. Defect Passivation via the Incorporation of Tetrapropylammonium Cation Leading to Stability Enhancement in Lead Halide Perovskite. *Adv. Funct. Mater.* **2020**, *30* (13), 1909737.
- 52. Xiong, J.; Dai, Z.; Zhan, S.; Zhang, X.; Xue, X.; Liu, W.; Zhang, Z.; Huang, Y.; Dai, Q.; Zhang, J. Multifunctional Passivation Strategy Based on Tetraoctylammonium Bromide for Efficient Inverted Perovskite Solar Cells. *Nano Energy* **2021**, *84*, 105882.
- 53. Zhang, T.; Xie, L.; Chen, L.; Guo, N.; Li, G.; Tian, Z.; Mao, B.; Zhao, Y. In Situ Fabrication of Highly Luminescent Bifunctional Amino Acid Crosslinked 2D/3D NH3C4H9COO(CH3NH3PbBr3)n Perovskite Films. *Adv. Funct. Mater.* **2017**, *27* (1), 1603568.
- 54. Ye, S.; Rao, H.; Zhao, Z.; Zhang, L.; Bao, H.; Sun, W.; Li, Y.; Gu, F.; Wang, J.; Liu, Z.; Bian, Z.; Huang, C. A Breakthrough Efficiency of 19.9% Obtained in Inverted Perovskite Solar Cells by Using an Efficient Trap State Passivator Cu(thiourea)I. *J. Am. Chem. Soc.* **2017**, 139 (22), 7504-7512.
- 55. Kyoungwon, C.; Junwoo, L.; Hong Il, K.; Cheol Woong, P.; Guan-Woo, K.; Hyuntae, C.; Sungjin, P.; Sang Ah, P.; Taiho, P. Thermally Stable, Planar Hybrid Perovskite Solar Cells with High Efficiency. *Energy Environ. Sci.* **2018**, (11), 3238-3247.

- 56. Yang, S.; Dai, J.; Yu, Z.; Shao, Y.; Zhou, Y.; Xiao, X.; Zeng, X. C.; Huang, J. Tailoring Passivation Molecular Structures for Extremely Small Open-Circuit Voltage Loss in Perovskite Solar Cells. *J. Am. Chem. Soc.* **2019**, *141* (14), 5781-5787.
- 57. Lee, J. W.; Tan, S.; Seok, S. I.; Yang, Y.; Park, N. G. Rethinking the A Cation in Halide Perovskites. *Science* **2022**, *375* (6583), eabj1186.
- 58. Abate, S. Y.; Huang, D.-C.; Tao, Y.-T. Surface modification of TiO2 layer with phosphonic acid monolayer in perovskite solar cells: Effect of chain length and terminal functional group. *Organic Electronics* **2020**, 78.
- 59. Qi, Y.; Ndaleh, D.; Meador, W. E.; Delcamp, J. H.; Hill, G.; Pradhan, N. R.; Dai, Q. Interface Passivation of Inverted Perovskite Solar Cells by Dye Molecules. *ACS Applied Energy Materials* **2021**, *4* (9), 9525-9533.
- 60. Qi, Y.; Green, K. A.; Ma, G.; Jha, S.; Gollinger, K.; Wang, C.; Gu, X.; Patton, D.; Morgan, S. E.; Dai, Q. Passivation of Iodine Vacancies of Perovskite Films by Reducing Iodine to Triiodide Anions for High-Performance Photovoltaics. *Chem. Eng. J.* **2022**, (438), 135647.
- 61. Glaser, T.; Muller, C.; Sendner, M.; Krekeler, C.; Semonin, O. E.; Hull, T. D.; Yaffe, O.; Owen, J. S.; Kowalsky, W.; Pucci, A.; Lovrincic, R. Infrared Spectroscopic Study of Vibrational Modes in Methylammonium Lead Halide Perovskites. *J. Phys. Chem. Lett.* **2015**, *6* (15), 2913-8.
- 62. Zhao, W.; Xu, J.; He, K.; Cai, Y.; Han, Y.; Yang, S.; Zhan, S.; Wang, D.; Liu, Z.; Liu, S. A Special Additive Enables All Cations and Anions Passivation for Stable Perovskite Solar Cells with Efficiency over 23. *Nano-Micro Lett.* **2021**, *13* (1), 169.

- 63. Ai, Y.; Zhang, Y.; Song, J.; Kong, T.; Li, Y.; Xie, H.; Bi, D. In Situ Perovskitoid Engineering at SnO2 Interface Toward Highly Efficient and Stable Formamidinium Lead Triiodide Perovskite Solar Cells. *J. Phys. Chem. Lett.* **2021**, *12* (43), 10567-10573.
- 64. Wang, R.; Xue, J.; Wang, K.-L.; Wang, Z.-K.; Luo, Y.; Fenning, D.; Xu, G.; Nuryyeva, S.; Huang, T.; Zhao, Y.; Yang, J. L.; Zhu, J.; Wang, M.; Tan, S.; Yavuz, I.; Houk, K. N.; Yang, Y. Constructive Molecular Configurations for Surface-Defect Passivation of Perovskite Photovoltaics. *Science* **2019**, *366*, 1509–1513
- 65. Kieslich, G.; Sun, S.; Cheetham, A. K. An Extended Tolerance Factor Approach for Organic-Inorganic Perovskites. *Chem. Sci.* **2015**, *6* (6), 3430-3433.
- 66. Gharibzadeh, S.; Abdollahi Nejand, B.; Jakoby, M.; Abzieher, T.; Hauschild, D.; Moghadamzadeh, S.; Schwenzer, J. A.; Brenner, P.; Schmager, R.; Haghighirad, A. A.; Weinhardt, L.; Lemmer, U.; Richards, B. S.; Howard, I. A.; Paetzold, U. W. Record Open-Circuit Voltage Wide-Bandgap Perovskite Solar Cells Utilizing 2D/3D Perovskite Heterostructure. *Adv. Energy Mater.* **2019**, *9* (21), 1803699.
- 67. Abate, S. Y.; Wu, W.-T.; Pola, S.; Tao, Y.-T. Compact TiO2 Films with Sandwiched Ag Nanoparticles as Electron-Collecting Layer in Planar type Perovskite Solar Cells: Improvement in Efficiency and Stability. *RSC Adv.* **2018**, *8* (14), 7847-7854.
- 68. Christians, J. A.; Manser, J. S.; Kamat, P. V. Best Practices in Perovskite Solar Cell Efficiency Measurements. Avoiding the Error of Making Bad Cells Look Good. *J. Phys. Chem. Lett.* **2015**, *6* (5), 852-7.
- 69. Huang, Y.; Li, L.; Liu, Z.; Jiao, H.; He, Y.; Wang, X.; Zhu, R.; Wang, D.; Sun, J.; Chen, Q.; Zhou, H. The Intrinsic Properties of FA(1-x)MAxPbI3 Perovskite Single Crystals. *J. Mater. Chem. A* **2017**, *5* (18), 8537-8544.

70. Kang, D.-H.; Kim, S.-Y.; Lee, J.-W.; Park, N.-G. Efficient Surface Passivation of Perovskite Films by a Post-Treatment Method with a Minimal Dose. *J. Mater. Chem. A* **2021**, *9* (6), 3441-3450.

# TOC

